

Dynamics and control of air turbines in oscillating-water-column wave energy converters: Analyses and case study



J.C.C. Henriques^{a,*}, J.C.C. Portillo^a, W. Sheng^b, L.M.C. Gato^a, A.F.O. Falcão^a

^a IDMEC, Instituto Superior Técnico, Universidade de Lisboa, Av. Rovisco Pais, 1049-001, Lisboa, Portugal

^b School of Engineering, University College Cork, Cork, Ireland

ARTICLE INFO

Keywords:

Wave energy
Oscillating water column
Wells turbine
Biradial turbine
Turbine control
Electrical generator

ABSTRACT

The paper presents a detailed analysis of the dynamics and control of air turbines and electrical generators in oscillating-water-columns (OWCs). The aim is to explain the performance of an OWC device based on the physical behaviour of each system component. The Mutriku wave power plant was chosen as the test case. The power plant is a breakwater located in the Bay of Biscay, in Basque Country, Spain. The contributions of the work are: i) development of a hydrodynamic model of the power plant in the frequency domain; ii) implementation of a non-linear time-domain wave-to-wire model; iii) real-valued implementation of the Prony method for the computation of the wave-radiation force; iv) a detailed generator model based on experimental data to assess the influence of the generator efficiency on the power take-off performance; v) a critical performance comparison of the Wells and biradial turbines; vi) a sensitivity analysis of the control parameters of the turbine/generator set; and vii) an explanation of the comparative performance of both turbines based on statistical data. The turbine performance curves were taken from developers' published experimental data. The results were obtained with a simplified model of the wave climate off the Mutriku test site comprising 14 sea states.

1. Introduction

Numerous wave power extraction concepts and technologies have been researched and developed to different maturity levels, especially in the last five decades [1–4]. This continues to be an active field of research and development. Understanding the complex and various phenomena associated with wave energy systems is essential to accomplish significant cost reductions in manufacturing, commissioning, operation and maintenance, and attain higher power generation.

The last decades have been devoted to seeking solutions in wave energy that are capable of offering cost-effective products/systems to do viable commercial projects. Nevertheless, wave energy project deployment, from concept to commercial stage, has been found to be a difficult, slow and expensive process [1]. Numerous spin-off and companies have failed and went bankrupt in this quest. Reasons for these failures are several. Nevertheless, it is necessary to leverage the knowledge about the technologies, their advantages and disadvantages.

The knowledge and understanding of systems and phenomena are of utmost importance, even when dealing with simplified models [5,6]. This type of models allows a better understanding of the physics of these complex systems. This is an important reason why all

contributions to assess and understand wave energy systems must be well-valued and critically considered. With the present technology, it should not be difficult to avoid costly mistakes due to the lack of knowledge on specific matters.

The scenarios and perception of the offshore renewable energy have changed substantially over the past decades, especially concerning wave energy conversion systems, as it is observed comparing references [7,8]. Barriers and drivers have also changed over time. Drivers have been found, in general, to be more associated to all three pillars of sustainability (economic, environmental and social) [9], while barriers are more associated to the difficulties of real deployments and economic unfeasibility of some projects. The difficulties of real deployments can be linked to political, regulatory and technical issues. Nevertheless, this is not an easy classification matter [9].

The present study is focused on technical aspects related to air turbines, electrical generators and the control of the power-take-off system (PTO) of oscillating water columns (OWCs). The aim is to explain the performance of an OWC device based on the physical behaviour of each system component. This knowledge is required to conceive OWC systems that can harvest as much ocean energy as possible.

The OWC is widely regarded as one of the simplest and most reliable

* Corresponding author.

E-mail addresses: joaochenriques@tecnico.ulisboa.pt (J.C.C. Henriques), juan.portillo@tecnico.ulisboa.pt (J.C.C. Portillo), wanan_sheng@outlook.com (W. Sheng), luis.gato@tecnico.ulisboa.pt (L.M.C. Gato), antonio.falcao@tecnico.ulisboa.pt (A.F.O. Falcão).

Nomenclature		<i>Greek symbols</i>
<i>Romans</i>		
a	generator control law constant	γ specific heat ratio of air, c_p/c_v [–]
A^∞	added mass at infinite frequency [kg]	F_1 excitation force on body 1 per [N/m] unit wave height
$A(\omega_m)$	wave amplitude as function of the wave frequency [m]	Δt time interval [s]
b	generator control law exponent	η_{turb} turbine efficiency [–]
c_{in}	speed of sound at turbine inlet conditions [m/s]	η_{elec} electrical efficiency [–]
CWR_{elec}	electrical capture width ratio [–]	ν kinematic viscosity of air [m^2/s]
CWR_{pneu}	pneumatic capture width ratio [–]	Π turbine dimensionless power [–]
CWR_{turb}	turbine capture width ratio [–]	ρ air density [kg/m^3]
D	turbine rotor diameter [m]	ρ_{at} air density in atmospheric conditions [kg/m^3]
F_{d1}	excitation force on body 1 [N]	ρ_{in} stagnation air density at turbine inlet [kg/m^3]
f_o	frequency of occurrence of a sea state [%]	ρ_w water density [kg/m^3]
g	acceleration of gravity [m/s^2]	Φ turbine dimensionless flow rate [–]
H_s	significant wave height [m]	ϕ_1 phase of body 1 response [rad]
I	turbine/generator set moment of inertia [kg m^2]	Ψ turbine dimensionless pressure head [–]
I_r	radiation state [–]	ω wave frequency [rad/s]
ℓ	air chamber width [m]	Ω turbine/generator set rotational speed [rad/s]
m_1	mass of body 1 [kg]	
\dot{m}_{turb}	turbine mass flow rate [kg/s]	
p	absolute air chamber pressure [Pa]	
p^*	dimensionless relative pressure [–]	<i>Superscripts</i>
P_{at}	absolute atmospheric pressure [Pa]	
P_{elec}	electrical power [W]	*
$P_{\text{lim}}^{\text{ctrl}}$	generator electromagnetic power [W]	dimensionless quantity
$P_{\text{rated}}^{\text{gen}}$	generator rated power [W]	limited value
P_{pneu}	pneumatic power, $\Delta p Q_{\text{turb}}$ [W]	maximum value
P_{turb}	turbine aerodynamic power [W]	rated quantity
\dot{P}_{wave}	wave energy flux per unit wave-crest length [W/m]	
Q_{turb}	turbine volumetric flow rate at inlet conditions [m^3/s]	<i>Subscripts</i>
R_1	radiation damping force on body 1 [N]	
S_1	OWC water plane area [m^2]	1 weightless rigid piston, denoted as body 1
t	time [s]	at atmospheric quantity
T_e	energy period [s]	bep best efficiency point
V_0	volume of air inside the chamber in calm water [m^3]	c chamber
V_c	instantaneous air chamber volume [m^3]	elec electrical quantity
u	safety valve control variable [0/1]	f final instant
v_1	velocity of body 1 [m/s]	gen generator quantity
z_1	vertical position body 1 [m]	i initial instant
		in turbine inlet conditions
		n sea state number
		pneu pneumatic value
		turb turbine quantity

and developed technologies and has the largest number of prototypes deployed into the sea [10–12]. Remarkably, the fixed-structure OWC installed at the Pico Island, Azores archipelago, operated from 1999 to 2017. Descriptions and reviews of the most common types of air turbines for OWCs can be found in Refs. [1,11,13,14]. The Wells turbine is the best known self-rectifying air turbine for wave energy applications and equipped most OWC prototypes, but there are others, mostly of axial impulse type [11,13,15,16]. An alternative type of turbine has been developed at Instituto Superior Técnico, Lisbon [17,18]: the biradial turbine is a novel impulse turbine with peak and time-average efficiencies higher than the first generation of self-rectifying air turbines [19]. This work studies and compares two types of air turbines for OWCs: the Wells and the biradial air turbine. Both turbines are assumed to have a valve installed in series with the rotor for control purposes.

Once a type of PTO is selected, it is necessary to establish control mechanisms and strategies to keep the power-take-off systems working as close as possible to their best efficiency points. It is essential to understand the dynamics of the integrated system to accomplish this objective.

Control strategies were developed over the last decades along with the wave energy technologies. Control of wave energy converters (WECs) presents particular challenges and can improve the overall

conversion efficiency by a factor up to three to five in random waves [5]. Control of a WEC seems to have been first implemented in 1970 during laboratory tests of the Edinburgh duck [5]. Falnes and Budal proposed phase control by latching in 1978 [20–22]. Special attention has been devoted to numerical investigations associated with latching control as an effective way of increasing the averaged power output of floating wave energy converters [23–25]. The built-in high-speed safety valve of the biradial turbine has raised the interest of latching control for OWCs [26–31]. The air compressibility allows the possibility of closing high-speed safety valve whenever required by the control method. Other types of control for OWCs can be found in Refs. [32–36]. Emerging strategies and implementation approaches for control of WECs can be found in Refs. [5,37–40]. A recent and interesting review about WECs control can be found in Ref. [41].

In the case of OWCs equipped with air turbines, the regulation of the turbine rotational speed strongly affects the power performance of the PTO and more weakly the OWC hydrodynamics [42]. Consequently, a way to enable the turbine to respond efficiently to a broader range of sea states is to use variable rotational speed [43–45]. Rotational speed control and the main variables that affect its implementation are considered and explained here, also serving as a base for discussion and comparison of the two turbines investigated.

The air turbine type and size, the control of the turbine rotational speed and the rated power of the electrical equipment have a substantial effect on the power performance of an OWC plant [43,46]. The present work arises due to the need to devise fair comparisons between air-turbines based on their performance and interactions with the integrated system under rotational speed control, based on physical insights and statistical treatment of observations. This is achieved through the study of two of the most researched and developed air turbines: Wells and biradial air turbines. This project involved the Mutriku OWC-breakwater wave power plant, where a biradial air turbine was installed in one of the 14 operational caissons. Other caissons are equipped with the original Wells turbines, which represent an interesting configuration for this work. The present paper was part of the R&D process undertaken during the preparation of a test campaign at Mutriku for the OPERA project (<http://opera-h2020.eu/>). The final goal of the OPERA project is the deployment the IDOM's OWC spar buoy at Biscay Marine Energy Platform infrastructure (BiMEP) with the aim of testing: the novel biradial air turbine, advanced turbine control strategies, elastomeric mooring tether, and shared mooring configuration. The contributions of the paper are:

- development of a frequency domain model of the Mutriku wave power plant;
- the implementation a non-linear time domain wave-to-wire model of the power plant including air chamber compressibility;
- the inclusion of a model of the turbine and generator efficiencies based on experimental data;
- a detailed analysis and comparison of the performance of Wells and biradial turbines for the Mutriku power plant;
- a real-valued implementation of the Prony method for the computation of the wave-radiation force;
- a sensitivity analysis of the parameters of the generator control law;
- an explanation of the performance of both turbines based on statistical data.

The paper is organised as follows. A description of the Mutriku site is provided in Section 2. Afterwards, the mathematical model is presented, which comprises the frequency domain model and the time domain wave-to-wire model described in Sections 3 and 4, respectively. Section 5 presents the results of the comparison of the Wells turbine versus the biradial turbine for the Mutriku wave power plant, from the perspective of the rotational speed control or feedback control, but accounting for the dynamic behavior inherent to the devices, the wave climate of Mutriku, and the sensitivity of the control parameters to the mean power output of both turbines. Conclusions appear in Section 6.

2. Mutriku OWC-breakwater

The Basque government constructed the first multi-OWC fixed-structure wave power plant in Europe. The power plant was inaugurated in July 2011, see (Fig. 1). The Mutriku breakwater is located in a fishing town with the same name in the province of Gipuzkoa, northern Spain. The civil construction works were executed during 2007–2008 [48]. During its construction, the breakwater was hit by storms in December 2007, March 2008, and January 2009 [49]. Several structural damages around the power plant resulted from the last storm. Currently, only 14 of the 16 chambers are operational.

The air chambers have the following dimensions: 4.5 m wide, 4.3 m long and 7.45 m high (above the maximum Equinoctial Spring Tide Low Water). Each chamber is equipped with a Wells turbine of 18.5 kW rated power. The plant's total installed capacity is 296 kW [47]. This is fed into the electrical grid. It is estimated that the wave power plant meets the household electricity requirements of approximately 100 homes.

2.1. Wave energy resource at Mutriku

The wave climate off the Mutriku power plant was represented by a set of 14 sea states, as described in Ref. [48] and in Table 1. The wave energy resource available at the Mutriku power plant was modelled using a spectrum defined by

$$S_{\text{Mut}}(\omega) = S_J(\omega) \varphi_{\text{Mut}}(\omega), \quad (1)$$

where ω is the angular frequency of the ocean waves, $S_J(\omega)$ is a JONSWAP spectra as described in Appendix A, and $\varphi_{\text{Mut}}(\omega)$ is an attenuation function which adjusts experimental near-shore ADCP data obtained at the Mutriku site [50], see Fig. 2.

The real waves were represented as a superposition of regular waves assuming the Mutriku wave spectrum, , where the amplitude of each wave component was computed as

$$A(\omega_m) = \sqrt{2 \Delta\omega_m} S_{\text{Mut}}(\omega_m). \quad (2)$$

The spectrum was discretized with non-uniform frequency spacing $\Delta\omega_m$. For further details see Ref. [51].

3. Mutriku frequency domain model

In the dynamic analysis of the Mutriku power plant, a hybrid frequency-time domain analysis was employed [52]. The first step of the numerical model was the frequency-domain analysis of the interaction between the power plant and waves. The relevant hydrodynamic



Fig. 1. Shoreline view of the Mutriku wave power plant [47].

Table 1

Characteristic wave climate measured off the Mutriku power plant. Each sea state, n , of the wave climate is defined by the significant wave height, H_s , energy period, T_e , and frequency of occurrence, f_o . Taken from Ref. [48].

n	H_s [m]	T_e [s]	f_o [%]
1	0.88	5.5	3.23
2	1.03	6.5	3.44
3	1.04	7.5	5.08
4	1.02	8.5	6.11
5	1.08	9.5	10.73
6	1.19	10.5	9.31
7	1.29	11.5	9.52
8	1.48	12.5	7.42
9	1.81	13.5	2.75
10	2.07	14.5	2.96
11	2.59	15.5	1.34
12	2.88	16.5	0.40
13	3.16	11.5	0.27
14	3.20	12.5	0.42

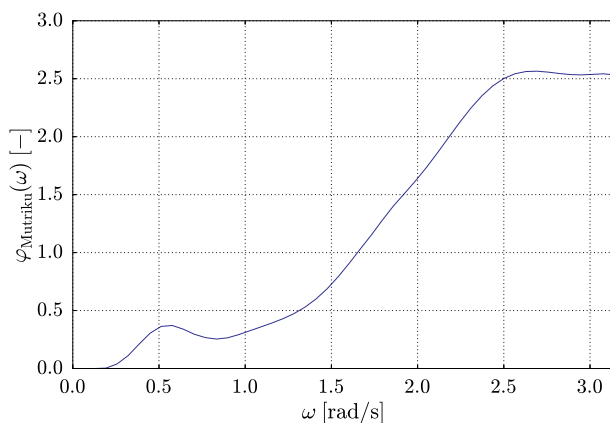


Fig. 2. Attenuation function used to adjust the offshore wave climate data to the Mutriku power plant site [50].

parameters were then transformed to time domain incorporating the air compressibility, the non-linear PTO system (turbine/generator) and the PTO control. In this section, the hydrodynamic coefficients that model the wave-structure interaction were obtained with the aid of a three-dimensional boundary element method in the frequency domain.

The hydrodynamic model of Mutriku comprised an approximate representation of the geometry of the plant, the seabed and the OWC itself. The first step was to create the surface geometry of the device, as depicted in (Fig. 3a). The approximation disregards the slight curvature of the breakwater planform shape (see Fig. 1). The model assumes a rectangular structure subject to normal incident waves. Only the three central air chambers were modelled, and the detailed computations were performed for the central one, as shown in Fig. 3.

The wetted surfaces are discretized in a three-dimensional mesh, as shown in (Fig. 3 b). Thin walls were approximated through dipole panels, and a thick piston approach was implemented to model the OWC [53]. The latter considers an imaginary, slightly submerged, rigid piston (denoted as body 1) modelled through source panels. The free surface above the piston was also discretized to avoid singularities in the solution. To account for intermediate and shallow water effects, the seabed was represented, over a distance of 200 m from the OWC chambers, as a sloping plane, with 15 m maximum depth and 5.65 m minimum depth at the breakwater wall (these are values at mean tide).

In the adopted Boundary Element Method (BEM) the basic assumptions are: the fluid is incompressible and the flow is irrotational. Since small amplitudes were assumed for the waves and body motions, the free-surface boundary conditions could be linearised. The WAMIT software was employed [54] to compute the frequency-dependent hydrodynamic coefficients $A_1(\omega)$ (added mass), $B_1(\omega)$ (radiation damping coefficient) and $\Gamma_1(\omega)$ (excitation force coefficient per unit wave amplitude).

The dimensionless added mass, $A_1^*(T)$, dimensionless damping, $B_1^*(T)$, dimensionless excitation force, $\Gamma_1^*(T)$, excitation force phase, $\phi_1(T)$, and the response amplitude operator (RAO) for heave are plotted, as functions of the wave period $T = 2\pi/\omega$, in Fig. 4a and b. The heave response curve (RAO) of the piston motion exhibits a peak at wave period of about 6 s, which is the resonance period of the piston heave motion. The most important feature of the Mutriku power plant is the resonance conditions found in the RAO for wave periods between 8 and 24 s. This is very different from the heave responses of a device in deep water, in which the response in very long waves is equal to unity, meaning the device is a wave-follower. However, for the Mutriku power plant, the water depth is relatively small, and so the wave amplitude is larger in the shallow water region due to the shoaling effect.

4. Mutriku time-domain wave-to-wire model

To get a deeper insight into the dynamics of an OWC WEC, it is fundamental to understand the interaction between the different components of the whole energy conversion system. The power conversion chain from the waves to the electrical grid is depicted in Fig. 5. The overall system dynamics can be understood as the interaction between the OWC hydrodynamics, the air chamber and the PTO sub-system.

4.1. OWC hydrodynamic modelling

The transformation from frequency-domain to time-domain follows the well-known Cummins [55] and Ogilvie [56] approach. Let z_1 be the heave motion coordinates of body 1, with $z_1 = 0$ at equilibrium position and the z -axis pointing upwards, see Fig. 6. The equations of motion for the OWC free-surface are

$$(m_1 + A_1^\infty) \dot{v}_1 = -\rho_w g S_1 z_1 - p_{at} S_1 p^* + F_{d1} - R_1, \quad (3a)$$

$$\dot{z}_1 = v_1. \quad (3b)$$

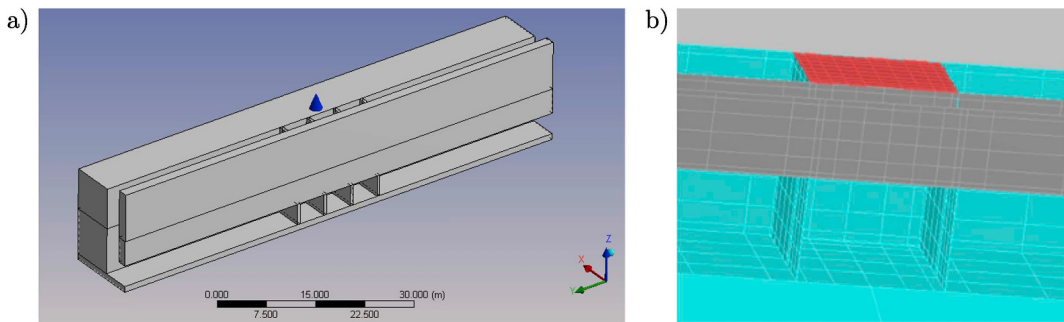


Fig. 3. a) Representation of the Mutriku wave power plant. b) Detail of the mesh of the central chamber.

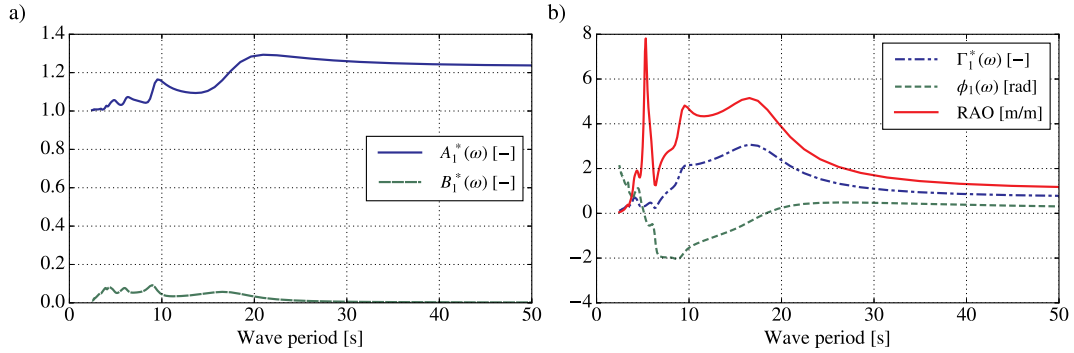


Fig. 4. a) Dimensionless added mass, $A_1^*(\omega) = A_1(\omega)/(\rho_w \ell^3)$, and dimensionless damping, $B_1^*(\omega) = B_1(\omega)/(\rho_w g^{1/2} \ell^{5/2})$, and ℓ is the air chamber width. b) Dimensionless excitation force, $\Gamma_1^*(\omega) = \Gamma_1(\omega)/(\rho_w g \ell^2)$, excitation force phase, $\phi_1(\omega)$, response amplitude operator (RAO) of the water column.

Here, the dot denotes time derivative, v_1 is the velocity of body 1, g is the acceleration of gravity, ρ_w is water density and the constant A_1^∞ is the added mass at infinite frequency. The internal air-water interface area is denoted by S_1 . The dimensionless relative pressure oscillation inside the chamber is defined as

$$p^* = \frac{p}{p_{at}} - 1, \quad (4)$$

where p_{at} is the atmospheric pressure, and p is the instantaneous absolute pressure oscillation inside the air chamber.

The excitation force acting on the imaginary piston is obtained as a sum of M components of frequency ω_m ,

$$F_{di} = \sum_{m=1}^N A(\omega_m) \Gamma_1(\omega_m) \cos(\omega_m t + \phi_1(\omega_m) + \phi_r(\omega_m)), \quad (5)$$

where $A(\omega_m)$ is given in Eq. (2), Γ_1 the piston heave excitation response, ϕ_r the excitation response to the wave component and ϕ_1 the phase in the wave generation (a uniform random phase). The radiation force is defined as $A_1^\infty \ddot{z}_1 + R_1$ where

$$R_1 = \int_0^t \kappa_1(t-s) v_1(s) ds, \quad (6)$$

and $\kappa_1(t)$ is the impulse function of the piston motion, which is the inverse Fourier transform of frequency dependent radiation damping $B_1(\omega)$. The convolution integral appearing in R was approximated using the Prony method [57,58]. In this approach, the convolution integral is computed using a linear state-space model where the kernel $\kappa_1(t)$ is approximated by a sum of N complex exponentials, giving

$$\dot{\mathbf{I}}_r = \beta_r \mathbf{I}_r + \alpha_r v_1. \quad (7)$$

and $R = \sum_{k=1}^N I_k$. In the present paper, $N = 16$ exponentials were used to approximate the kernel κ_1 , as shown in Fig. 7. To avoid a complex time integrator, the solution of Eq. (7) uses a new real-valued implementation described in Appendix B.

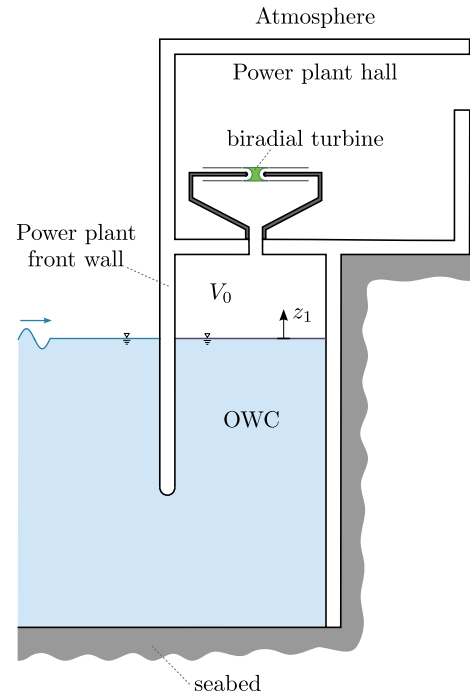


Fig. 6. Schematic cross section view of one of the chambers of the Mutriku power plant with the biradial turbine installed (not to scale).

4.2. Air chamber pressure modelling

Assuming an isentropic compression/expansion, the pressure in the air chamber is related to the mass flow rate of air through the turbine, \dot{m}_{turb} , (positive for outward flow), through

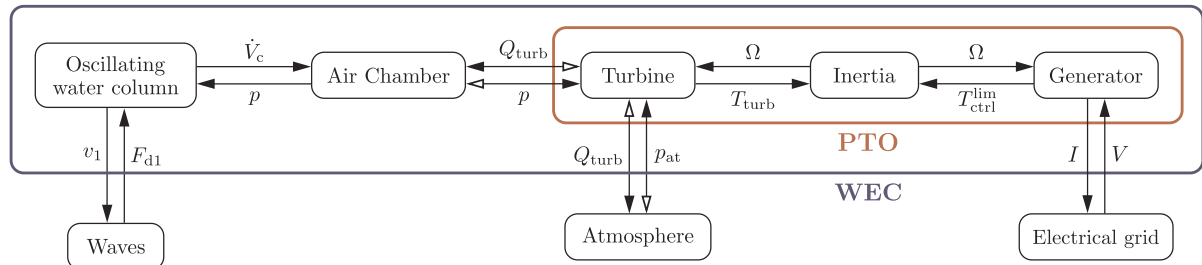


Fig. 5. Wave-to-wire power-flow on an OWC wave energy converter. The bidirectional power-flow between the air chamber, the turbine and the atmosphere is represented by double arrows. In the figure, V and I stand for voltage and electrical current, respectively.

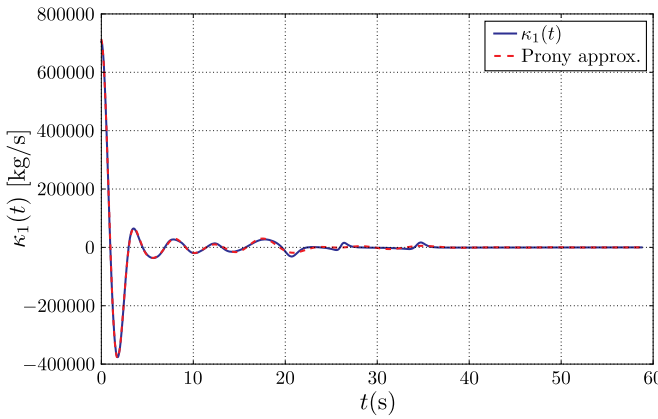


Fig. 7. Fitting of the impulse response function, $\kappa_1(t)$, with a sum of $N = 16$ exponentials.

$$\frac{\dot{p}^*}{p^* + 1} = -\gamma \left(\frac{\dot{V}_c}{V_c} + \frac{\dot{m}_{turb}}{m_c} \right), \quad (8)$$

where $V_c = V_0 - S_1 z_1$ is the instantaneous air chamber volume, V_0 is the air chamber volume in hydrostatic conditions, $m_c = \rho_c V_c$ is the instantaneous mass inside the air chamber, ρ_c denotes the air density inside the air chamber computed as

$$\rho_c = \rho_{at}(p^* + 1)^{1/\gamma}, \quad (9)$$

assuming an isentropic compression/expansion, and γ is the specific heat ratio; see Refs. [28,29,59] for further details.

4.3. Power take-off system

4.3.1. Turbine/generator set modelling

The dynamics of the turbine/generator set was modelled using

$$\frac{d}{dt} \left(\frac{1}{2} I \Omega^2 \right) = P_{turb} - P_{ctrl}, \quad (10)$$

where Ω , I , P_{turb} and P_{ctrl} are the turbine rotational speed, the moment of inertia of the rotating parts, the instantaneous turbine aerodynamic power (aerodynamic torque on the rotor times rotational speed), and the instantaneous generator electromagnetic power imposed to control the rotational speed, respectively.

The Wells turbines installed at Mutriku power plant have a diameter of 0.75 m, and a rotational inertia of 3.06 kg m² [60]. The biradial turbine installed within the H2020 OPERA project at the same power plant has a diameter of 0.50 m and a rotational inertia of 5.01 kg m². The data is summarized in Table 2.

4.3.2. Turbine modelling

For large Reynolds numbers $Re = \Omega D^2 / \nu > 10^6$ and low Mach numbers $Ma = \Omega D / c_{in} < 0.3$, the performance characteristics of air turbines can be presented in dimensionless form [61,62], as functions of the dimensionless pressure head Ψ ,

$$\Phi = f_\phi(\Psi), \quad (11)$$

$$\Pi = f_{\Pi}(\Psi), \quad (12)$$

where

$$\Psi = \frac{\Delta p}{\rho_{in} \Omega^2 D^2}, \quad (13)$$

$$\Phi = \frac{\dot{m}_{turb}}{\rho_{in} \Omega D^3}, \quad (14)$$

$$\Pi = \frac{P_{turb}}{\rho_{in} \Omega^3 D^5}. \quad (15)$$

Here Φ is the dimensionless flow rate, Π is the power coefficient, $\Delta p = p_{at} - p^*$ is the stagnation pressure head between the air chamber and the atmosphere, ρ_{in} is the turbine inlet density at stagnation conditions, Ω is rotational speed of the turbine, and D is the rotor diameter. The functions $f_{\Pi}(\Psi)$ and $\eta(\Psi)$ are even and the function $f_\phi(\Psi)$ is odd.

The turbine efficiency is defined as the output aerodynamic power divided by the available pneumatic power, P_{pneu} ,

$$\eta_{turb} = \frac{P_{turb}}{P_{pneu}} = \frac{\Pi}{\Phi \Psi} = \frac{f_{\Pi}(\Psi)}{f_\phi(\Psi) \Psi}, \quad (16)$$

where $P_{pneu} = \Delta p Q_{turb}$, and $Q_{turb} = \dot{m}/\rho_{in}$ is the turbine volumetric flow rate at inlet conditions.

The reference density, ρ_{in} , is a function of the pressure difference between the atmosphere and the air chamber. The processes of inhalation and exhalation require different approaches to the reference density, as shown below:

$$\rho_{in} = \begin{cases} \rho_c, & \text{if } p^* > 0 \text{ (exhalation)} \\ \rho_{at}, & \text{if } p^* \leq 0 \text{ (inhalation)} \end{cases}, \quad (17)$$

or, in a more compact form,

$$\rho_{in} = \max(\rho_c, \rho_{at}), \quad (18)$$

as a result of Eq. (9).

The turbine aerodynamic power is computed from Eqs. (15) and (16)

$$P_{turb} = \rho_{in} \Omega^3 D^5 f_{\Pi}(\Psi). \quad (19)$$

Here it is assumed that a safety valve is installed in series with the turbine. The binary variable u represents the controller action such that in normal operation the valve is open ($u = 1$), and if the PTO system is operating in safe mode then the valve is closed ($u = 0$), see sub-section 4.3.3 for details.

The Wells turbine installed at the Mutriku power plant has a butterfly valve installed in the duct that connects the turbine to the air chamber. The biradial turbine has a simple axially sliding built-in high-speed safety valve with a diameter slightly larger than the rotor diameter. The typical stroke of the valve is less than one-tenth of the rotor diameter.

The performance curves for the Wells and biradial turbines are plotted in Fig. 8a and b. The figures reveal that the biradial turbine has a larger range of operation with high-efficiency in comparison with the Wells turbine. This characteristic is even more visible when the turbines power, P_{turb} , is mapped as a function of the pressure head, Δp , and rotational speed, Ω , see Fig. 8c and d. For computing these maps, the diameters were those of the turbines installed at the Mutriku power plant Table 2. The maps show the larger operating range of the biradial turbine in comparison with the Wells turbine. In most of the area plotted in Fig. 8c, the Wells turbine has an output power almost negligible, i.e., smaller than 2.7 kW. Moreover, the maps also demonstrate that the biradial turbine performance is much less sensitive to the rotation speed variations. This conclusion is drawn from Fig. 8d where the

Table 2

Characteristics of the biradial and Wells turbines installed at Mutriku power plant and the base cases parameters a_{bep} and b used for the numerical analysis.

	Wells		Biradial	
	Installed & base case	Installed	Base case	
Diameter, D_{ref}	0.75	0.50	0.65	[m]
Inertia, I_{ref}	3.06	5.01	18.6	[kg m ²]
P_{gen}^{rated}	18.5	30.0	18.5	[kW]
Ψ_{bep}	0.0634	0.357	0.357	[–]
a_{ref}	2×10^{-4}	1×10^{-3}	3.7×10^{-3}	[W s ^b]
b	3	3	3	[–]

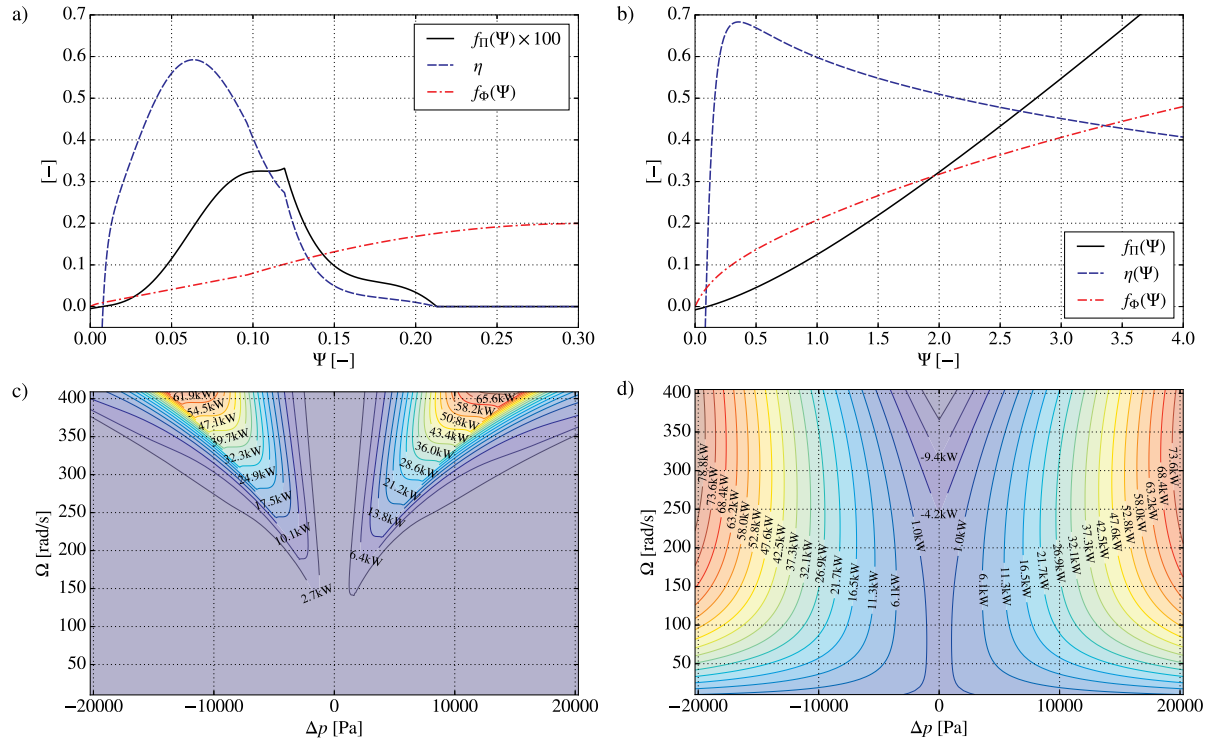


Fig. 8. Dimensionless flow rate, Φ , power coefficient, Π , and efficiency, η_{turb} , as functions of the dimensionless pressure head, Ψ , for the biplane Wells turbine a) and the biradial b) used in the numerical simulations, from Refs. [63,64]. Figs. c) and d) plot the turbine output power as function of the pressure head and rotational speed using the dimensionless $\Pi(\Psi)$ curves from a) and b), respectively.

isolines of turbine power are almost vertical from 150 to 400 rad/s.

4.3.3. Electrical generator modelling and control

Several generator control laws have been proposed for OWCs. One of the simplest and most effective control laws can be derived from simple physical arguments. Let us consider the limiting case when the inertia I is zero. In this case, Eq. (10) shows that the instantaneous torque transmitted at the generator shaft is equal to the instantaneous electromagnetic torque. If the goal is to maximize the turbine efficiency, then the turbine is to be operated at the best efficiency point Ψ_{bep} , and the turbine power should be proportional to

$$P_{\text{turb}}(\Psi_{\text{bep}}, \Omega) = \underbrace{\rho_{\text{in}} D^5 f_{\Pi}(u\Psi_{\text{bep}})}_{a_{\text{bep}} \approx \text{const}} \Omega^3, \quad (20)$$

where a_{bep} is nearly constant since the relative variations in the density ρ_{in} are small in comparison with the relative variations in rotational speed. As such, the generator power control should follow the relation

$$P_{\text{ctrl}} = a_{\text{bep}} \Omega^3, \quad (21)$$

to maximize the turbine power output.

In practice, if the inertia is not small and the coupling between the turbine aerodynamics and the OWC hydrodynamics is taken into account, we can use a more general relationship of the type [44]

$$P_{\text{ctrl}} = a \Omega^b. \quad (22)$$

Usually, the electrical generators are connected to the grid through a variable frequency drive (back-to-back power converter) controlled in torque mode. As such, the following limited control law was adopted based on torque

$$T_{\text{ctrl}}^{\lim} = \min\left(a \Omega^{b-1}, \frac{P_{\text{gen}}^{\text{rated}}}{\Omega}, T_{\text{gen}}^{\max}\right), \quad (23)$$

where $P_{\text{gen}}^{\text{rated}}$ is the rated (maximum allowed) power of the generator and T_{gen}^{\max} is the maximum allowed torque. Control law Eq. (23) was defined to avoid overloading the generator. The limited control law in terms of power yields

$$P_{\text{ctrl}}^{\lim} = \min(a \Omega^b, P_{\text{gen}}^{\text{rated}}, T_{\text{gen}}^{\max} \Omega). \quad (24)$$

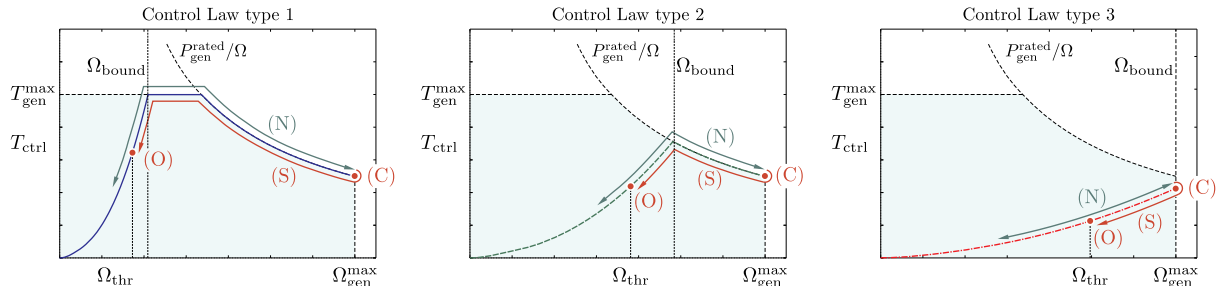


Fig. 9. Types of control law used in the simulations. The green shaded area represents the allowed operating region of the generator control laws as a function of the torque and rotational speed. The following notation was used: (N) ≡ normal operation, (C) ≡ close valve, (S) ≡ safety mode (valve closed), and (O) ≡ open valve (resume to normal operation). For plotting the control laws it was assumed that $\Omega_{\text{ctrl}}^{\max} = \Omega_{\text{gen}}^{\max}$, see Eq. (25).

which is valid even when the rotational speed is zero. As such, we can model the turbine self-starting if the asymptotic behaviour of $\Pi(\Psi)$ and $\Phi(\Psi)$ is known when $\Psi \rightarrow \infty$.

The rotational speed of the electrical generator is limited to a maximum value, $\Omega_{\text{gen}}^{\max}$, to ensure that the centrifugal stresses do not exceed the maximum allowed. On the other hand, the Mach number based on the tip speed must be limited to avoid flow compressibility effects on the turbine rotor blades such as shock waves [65]. Assuming a maximum blade tip-speed of $\Omega D/2 = 160$ m/s, the maximum rotational speed of the turbine/generator set is limited to

$$\Omega_{\text{ctrl}}^{\max} = \min(\Omega_{\text{gen}}^{\max}, 320 D^{-1}), \quad (25)$$

If the instantaneous rotational speed Ω exceeds $\Omega_{\text{ctrl}}^{\max}$ the control will enter in safety mode. Note that the Mach number effects are not related to the air chamber compressibility modelled by Eq. (8).

Fig. 9 depicts the three types of control laws that arise from the three imposed constraints, namely: the generator rated power, the maximum torque and the maximum rotational speed. For plotting the control laws of Fig. 9 it was assumed that $\Omega_{\text{ctrl}}^{\max} = \Omega_{\text{gen}}^{\max}$ without loss of generality. The shaded green area represents the allowed generator operating region. For the case of control law type 1, the first constraint to be reached is the maximum torque. After hitting this constraint, the control law follows the upper boundary of the shaded area until the maximum rotational speed, $\Omega_{\text{ctrl}}^{\max}$, is reached and the turbine control enters in safety mode. During safety mode operation, the valve is closed, $u = 0$, and normal operation is resumed when the rotational becomes lower than a given threshold, Ω_{thr} . This threshold is defined as follows. Let Ω_{bound} be the rotational speed value of the intersection of the exponential part of the control, Eq. (23), with the boundary of the allowed operating region, see Fig. 9. The control power at this rotational speed is $P_{\text{bound}} = \alpha \Omega_{\text{bound}}^b$. The adopted threshold is the value of rotational speed when the power is half of P_{bound} , giving

$$\Omega_{\text{thr}} = 2^{-1/b} \Omega_{\text{bound}}. \quad (26)$$

During safety mode operation, the control law Eq. (23) continues to be applied.

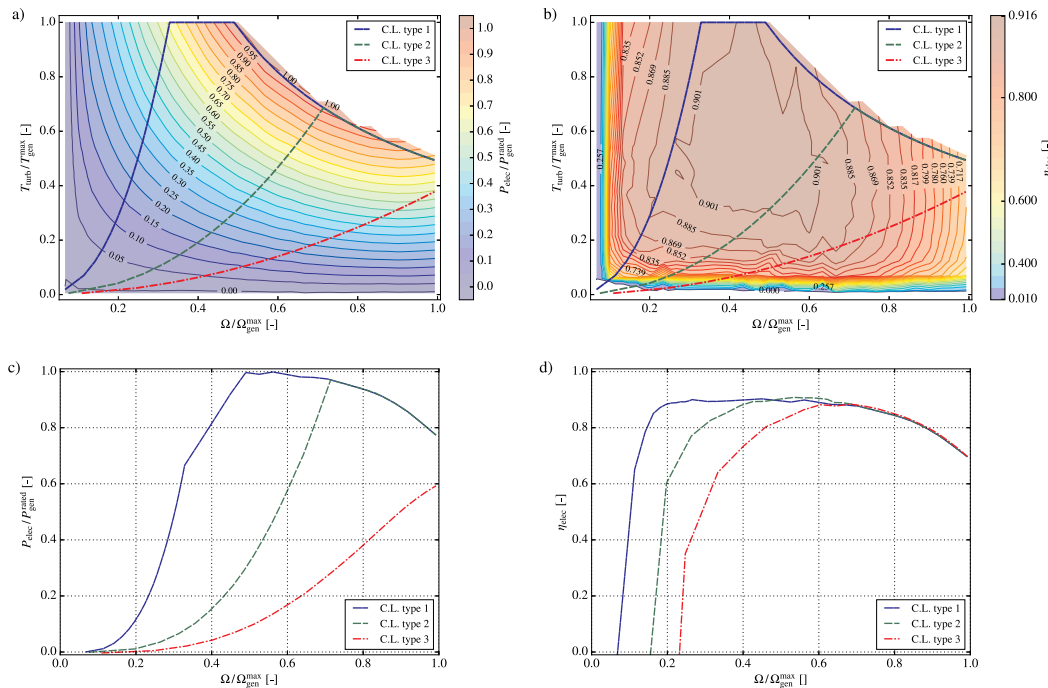


Fig. 10. Generator performance map as measured at the IST laboratory [64,66]. a) Generator electrical output power, P_{gen} , and b) generator electrical efficiency, η_{elec} , as a function of the rotational speed, Ω , and turbine aerodynamic power, T_{turb} . c) Generator electrical power output and d) generator efficiency along the path of control laws type 1, 2 and 3. For plotting the control laws it was assumed that $\Omega_{\text{ctrl}}^{\max} = \Omega_{\text{gen}}^{\max}$, see Eq. (25).

For control laws of types 2 and 3 illustrated in Fig. 9, the behaviour similar to the control law type 1, differing only in the first constraint to be hit. In the case of control law type 2, the generator rated power is the first constraint, while the rotational speed, $\Omega_{\text{ctrl}}^{\max}$, is the constraint of control law of type 3.

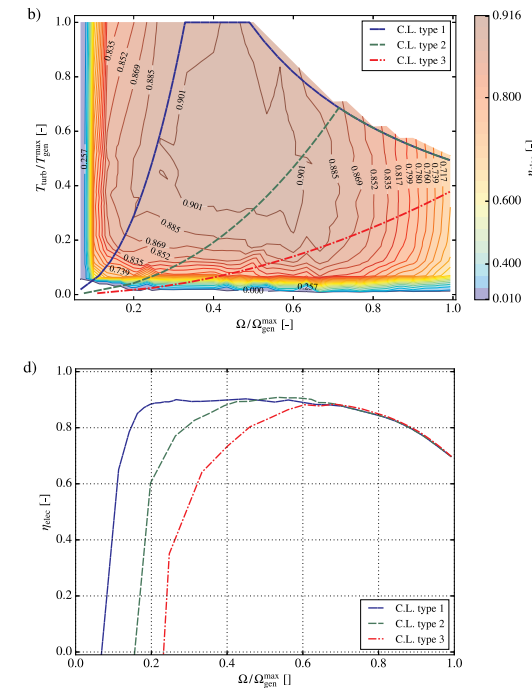
Within the H2020 OPERA project, IST team conducted a series of experiments to measure the efficiency of a SIEMENS IEC squirrel-cage low-voltage electrical generator, model 1LE1603-2AB53-4GB4-Z, under steady-state conditions [64,66]. This generator has a rated power of $P_{\text{gen}}^{\text{rated}} = 30.0$ kW at a nominal speed of $\Omega_{\text{gen}}^{\text{nom}} = 1470$ rpm, and a maximum rotational speed of $\Omega_{\text{gen}}^{\max} = 3000$ rpm. The torque at rated power and nominal speed was assumed to be the maximum allowed value $T_{\text{gen}}^{\max} = 216.5$ Nm.

Fig. 10a and b depict the dimensionless maps of electrical power output, $P_{\text{elec}}/P_{\text{gen}}^{\text{rated}}$, and generator electrical efficiency,

$$\eta_{\text{elec}} = \frac{P_{\text{elec}}}{P_{\text{turb}}}, \quad (27)$$

obtained as functions of the dimensionless turbine aerodynamic power, $T_{\text{turb}}/T_{\text{gen}}^{\max}$, and dimensionless rotational speed, $\Omega/\Omega_{\text{gen}}^{\max}$. In the maps are also plotted examples of the three types of control laws. Fig. 10c and d show that the selected control law has a major impact on the electrical power output and generator efficiency. The selection of the generator should allow the operation of the turbine control along curves where the generator has a good efficiency within a broad range of rotational speeds. This is the case of control law of type 1.

In the absence of the operating maps of the generator used in the Wells turbines installed at the Mutriku OWC-breakwater, the following approximation was used: the dimensionless maps of the Mutriku generator, Fig. 10a and b, are assumed equal to the 30 kW Siemens generator tested at IST. The non-dimensionless maps are scaled using the new rated power of $P_{\text{gen}}^{\text{rated}} = 18.5$ kW, a maximum rotational speed $\Omega_{\text{gen}}^{\max} = 4000$ rpm. The maximum torque is computed assuming a ratio of torques based on the maximum values of rated power and rotational speed



$$T_{\text{gen}}^{\max}|_{18.5 \text{ kW}} = \left(\frac{P_{\text{gen}}^{\text{rated}}}{\Omega_{\text{gen}}^{\max}} \right) \Big|_{18.5 \text{ kW}} \left(\frac{\Omega_{\text{gen}}^{\max}}{P_{\text{gen}}^{\text{rated}}} \right) \Big|_{30.0 \text{ kW}} T_{\text{gen}}^{\max}|_{30.0 \text{ kW}}. \quad (28)$$

For computational purposes, the curves plotted in Fig. 10c are used to compute the electrical output power as a function of the rotational speed. As such, the interpolation in the generator map, Fig. 10a, can be performed at once before the time-integration.

4.4. Hydrodynamic damping and power take-off system dynamics

To show the effect of the pressure on the volume flow rate Q_{OWC} displaced by the motion of the free surface inside the air chamber, Eq. (8) can be rewritten as

$$Q_{\text{OWC}} = \frac{V_c \dot{p}}{\gamma p} + K \frac{\Delta p}{\rho_c}, \quad (29)$$

where the turbine damping is defined as

$$K = \frac{\dot{m}_{\text{turb}}}{\Delta p}. \quad (30)$$

Note that Q_{OWC} is positive for upward motion, $Q_{\text{OWC}} = -\dot{V}_c$.

The Wells turbine is known to exhibit a linear relationship between the pressure head coefficient, Ψ , and the flow coefficient, Φ ,

$$\Psi = \kappa_W \Phi, \quad (31)$$

where κ_W is a dimensionless constant that depends only on turbine geometry but not on turbine size, rotational speed or fluid density. From the available experimental data [63], the Wells turbine installed at Mutriku power plant is non-linear for Ψ greater than 0.1, as found in Fig. 8a. Within the linear region, $0 \leq \Psi \leq 0.1$, the turbine damping, Eq. (30), can be computed using

$$K_W = \frac{D}{\kappa_W \Omega}. \quad (32)$$

In contrast, experimental tests revealed that the biradial turbine is characterized by a dimensionless relationship between pressure head and flow rate that can be fairly well approximated by Ref. [64].

$$\Psi = \kappa_B \Phi^{5/3}, \quad (33)$$

where κ_B is a dimensionless constant, see Fig. 8b). By using Eqs. (13) and (14) we get the biradial turbine damping

$$K_B = \frac{1}{\kappa_B^{3/5}} \frac{D^{9/5}}{\Omega^{1/5}} \left(\frac{\rho_{\text{in}}}{\Delta p} \right)^{2/5}. \quad (34)$$

From Eqs. (32) and (34) we find that:

- The biradial turbine damping is strongly affected by the rotor diameter and weakly influenced by the rotational speed ($K_B \propto D^{9/5} \Omega^{-1/5}$).
- The Wells turbine damping is a linear function of the rotor diameter and decreases when the rotational speed increases ($K_W \propto D \Omega^{-1}$).
- The biradial turbine damping decreases when the available pressure increases ($K_B \propto \Delta p^{-2/5}$). This effect is favourable to the turbine performance since the biradial turbine operates better when the available pressure is higher.
- The Wells turbine damping does not depend on the available pressure.
- Due to variations in the inlet density, when the flow is from the air chamber to the atmosphere, the inlet density slightly increases the biradial turbine damping but does not influence the Wells turbine ($K_B \propto \rho_{\text{in}}^{2/5}$).

The control of the rotational speed can be analysed expanding Eq. (10)

$$\frac{d}{dt} \left(\frac{1}{2} \Omega^2 \right) = \frac{1}{I} (\rho_{\text{in}} \Omega^3 D^5 f_{\Pi}(u\Psi) - \min(a\Omega^b, P_{\text{gen}}^{\text{rated}}, T_{\text{gen}}^{\max} \Omega)). \quad (35)$$

Eq. (35) shows that the state of the PTO system, Ω , is a function of the following design parameters:

- turbine/generator set inertia I ;
- turbine characteristic dimension D ;
- the operation of the turbine safety valve u as a function of the maximum rotational speed $\Omega_{\text{gen}}^{\max}$ and rotational speed threshold Ω_{thr} ;
- generator control parameters a and b ;
- electrical power limit of the generator $P_{\text{gen}}^{\text{rated}}$;
- generator maximum torque T_{gen}^{\max} .

The coupling between the system components is non-linear. However, the usual computation of the turbine damping in the frequency domain has been oversimplified by numerous authors, see Fig. 5. The results section aims to discuss and analyse the effect of these parameters on the turbine dynamics and power output and, ultimately, in the time-averaged electrical power output

$$\bar{P}_{\text{elec}} = \frac{1}{t_f - t_i} \int_{t_i}^{t_f} P_{\text{elec}}(\Omega(t)) dt, \quad (36)$$

in the time interval from t_i to t_f , where $P_{\text{elec}}(\Omega(t))$ is a function as shown in Fig. 10 c. Note that the electrical power can also be computed from the generator efficiency as $P_{\text{elec}}(t) = \eta_{\text{elec}}(\Omega(t)) P_{\text{turb}}(t)$.

5. Results and discussion

The performance comparison between the Wells turbine and the biradial turbine for the Mutriku power plant was performed based on the time domain model described in Section 4. Simulations were performed for all sea states described in Table 1 that characterise the Mutriku wave climate. The annual-averaged pneumatic, turbine and generator powers were computed based on the frequency of occurrence of sea states of the wave climate. For each sea state, the simulations were performed for a time interval of $t_f = 3600$ s with a time step of $\Delta t = 0.1$ s. To reduce the transient span associated to the initial conditions, the time-averaged values were computed from $t_i = 200$ s to t_f .

5.1. Optimal turbine diameter

The optimal turbine diameter for the Mutriku power plant is a function of the turbine damping as discussed in section 4.4, see Eqs. (29), (32) and (34).

For the present analysis, we use the generator control law as given by Eq. (24), with $a = a_{\text{bep}}$ and $b = 3$, see Eq. (21). The influence of a and b on the turbines performance is discussed in section 5.2.

For the turbine diameter assessment, we need to scale the turbine inertia I and the generator control parameter a_{bep} with the rotor diameter D . From geometric similarity $I \propto \rho_{\text{rotor}} D^5$, the turbine inertia is scaled as

$$I = I_{\text{ref}} \left(\frac{D}{D_{\text{ref}}} \right)^5. \quad (37)$$

Here it is assumed that the rotor density ρ_{rotor} is independent of rotor diameter and the reference characteristics are taken from the turbines tested at the Mutriku power plant, see Table 2.

From Eq. (20), we find that the coefficient a of the generator control law follows the same scaling as the inertia

$$a = a_{\text{ref}} \left(\frac{D}{D_{\text{ref}}} \right)^5. \quad (38)$$

For large Reynolds number, the dimensionless turbine characteristics κ_W , Eq. (31), and κ_B , Eq. (33), only depend on the turbine geometry but not on the rotor diameter. Two generators with different rated powers

were considered: 18.5 kW and 30 kW. These values correspond to the rated powers of the biradial and Wells turbines installed at Mutriku, see Table 2.

Fig. 11 plots the annual-averaged values of a) pneumatic capture width ratio, b) turbine capture width ratio, c) electrical capture width ratio, and d) turbine efficiency, as functions of the turbine diameter. Results are depicted for the biradial and Wells turbines considering two generator rated powers, 18.5 kW and 30.0 kW. The annual-averaged values were computed based on the Mutriku wave climate. The pneumatic capture width ratio is defined as

$$\text{CWR}_{\text{pneu}} = \frac{\bar{P}_{\text{pneu}}}{\hat{P}_{\text{wave}} \ell}, \quad (39)$$

where

$$\bar{P}_{\text{pneu}} = \frac{1}{t_f - t_i} \int_{t_i}^{t_f} P_{\text{pneu}}(t) dt, \quad (40)$$

denotes the time-averaged pneumatic power,

$$\hat{P}_{\text{wave}} = \sum_{m=1}^N \frac{\rho_w g^2 A(\omega_m)^2}{4 \omega_m}, \quad (41)$$

is wave energy flux per unit wave-crest length of the considered discrete sea spectrum and ℓ denotes the air chamber width. The capture width ratio (CWR) is a consensual measure of the conversion of energy ‘efficiency’ from the waves to the considered component. The turbine capture width and the electrical capture width are defined as

$$\text{CWR}_{\text{turb}} = \bar{\eta}_{\text{turb}} \text{CWR}_{\text{pneu}}, \quad (42)$$

$$\text{CWR}_{\text{elec}} = \bar{\eta}_{\text{elec}} \bar{\eta}_{\text{turb}} \text{CWR}_{\text{pneu}}, \quad (43)$$

respectively. The time-averaged turbine efficiency and electrical efficiency are computed as

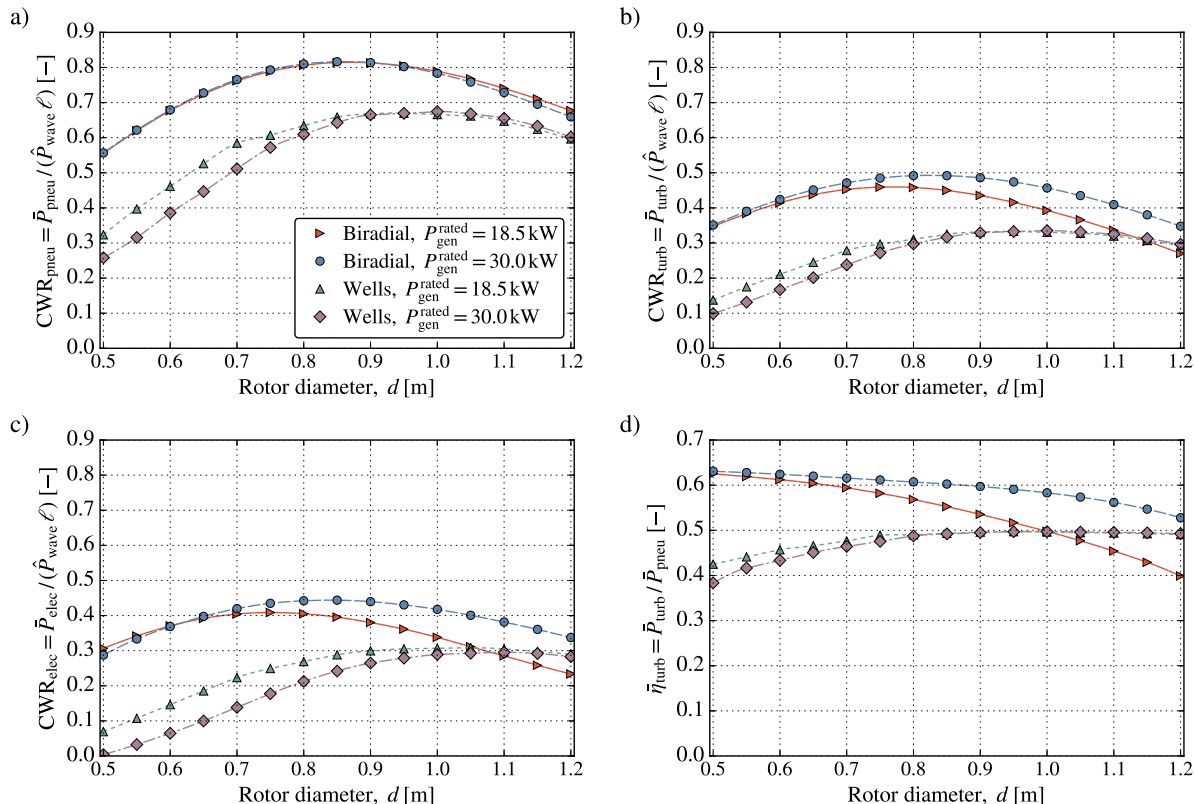


Fig. 11. Annual-averaged values of: a) pneumatic capture width ratio, b) turbine capture width ratio, c) generator capture width ratio, and d) turbine efficiency, as a function of the turbine diameter. Results are depicted for the biradial and Wells turbines considering two generator rated powers, 18.5 kW and 30.0 kW.

$$\bar{\eta}_{\text{turb}} = \frac{\bar{P}_{\text{turb}}}{\bar{P}_{\text{pneu}}}, \quad (44)$$

$$\bar{\eta}_{\text{elec}} = \frac{\bar{P}_{\text{elec}}}{\bar{P}_{\text{turb}}}. \quad (45)$$

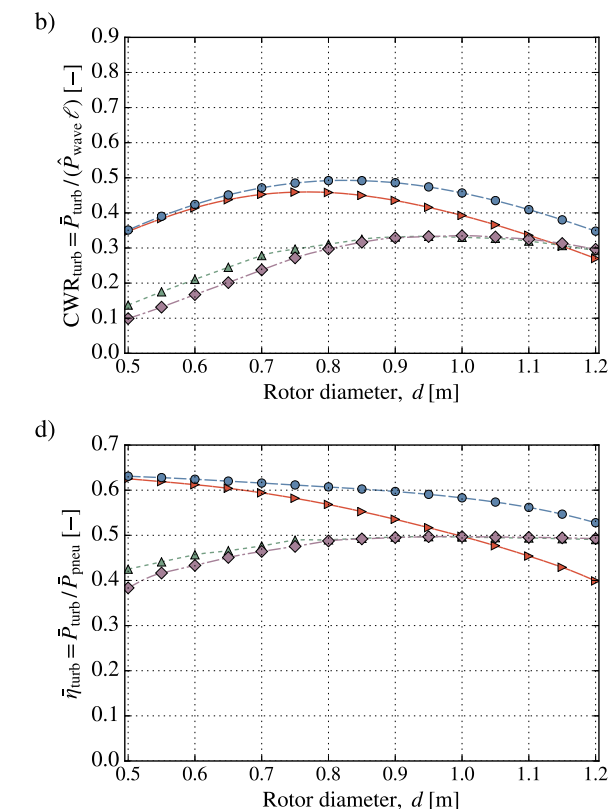
The time-averaged turbine power output, \bar{P}_{turb} , is computed similarly to \bar{P}_{pneu} , see Eq. (40).

From Fig. 11a and b we found that the optimal turbine diameter for the biradial turbine is about 0.85 m, and the curves have parabolic shape around the maximum. For the Wells turbine, the analysis of the plots shows that the optimal diameter is about 0.9 m for a rated power of 18.5 kW, and the curves around the optimal diameter are rather flat due to the constraints imposed by the control law.

For the Wells turbine, the very low capture width ratio for small diameters is a consequence of turbine damping becoming too low, and also of the imposed rotational speed limit. The dependence of the rotational speed on the turbine diameter is as follows. For a given pressure head, Δp , the value of ΩD must be constant for operation at the best efficiency point, $(\Omega D)^2 = \Delta p / (\rho_{\text{in}} \Psi_{\text{bep}})$, see Eq. (13). As the rotor diameter decreases, the rotational speed increases promoting the closure of the safety valve thus reducing the turbine power output. As the Wells turbine damping depends on the rotational speed, the pneumatic power is also affected, see sub-section 5.3 for further details.

As the biradial turbine damping is weakly affect by the rotational speed, the difference in the CWR_{pneu} between case of $P_{\text{gen}}^{\text{rated}} = 30.0 \text{ kW}$ and $P_{\text{gen}}^{\text{rated}} = 18.5 \text{ kW}$ is small, as seen in Fig. 11a. Another effect is the relatively low sensitivity of the results with respect to the generator rated power for the biradial turbine.

On what concerns the turbine efficiency, the biradial turbine has a rather flat response in comparison with the Wells turbine. The average efficiency of the biradial turbine increases with the decrease of the turbine diameter. This behaviour mainly results from the reduction in



turbine rotor inertia, see section 5.3. The control law of Eq. (21) allows the operation of the turbine closer, on average, to the best efficiency point. Since the biradial turbine operates at about half of the rotational speed of the Wells turbine [19], the safety valve is operated fewer times, in comparison with the Wells turbine.

The Wells turbine rotor diameter of 0.75 m installed at the Mutriku power plant is a good trade-off between cost and power output. In the case of the biradial turbine, a rotor diameter of 0.65 m seems to be a reasonable balance between cost and performance. These two rotor diameters will be used for further comparisons between the Wells and the biradial turbines and will be denoted as the base case, see Table 2.

Comparing the base cases, the CWR_{elec} of the Wells turbine is 59% less than the biradial turbine ($CWR_{elec}^{Wells}=0.244$ and $CWR_{elec}^{\text{biradial}}=0.388$). This is the most important capture width ratio since it measures the wave-to-wire efficiency. Note that in this analysis the efficiency of the variable-frequency driver was not taken into account. This electrical component is expected to have an efficiency higher than that of the generator.

Fig. 12a and b give further insight into the effect of the turbine diameter on the overall performance of the turbine. In the figures the time-averaged turbine power output is presented for the sea states of the Mutriku wave climate for the base cases. For comparison, it is shown how the turbine power output varies with a change of ± 0.1 m in the turbine rotor diameter with respect to the base case. For both turbines, the turbine power output has a small sensitivity to the changes on the rotor diameter for the most frequent sea state (SS5). For more energetic sea states, the extracted energy increases with the increase of the rotor diameter. In the case of the lower energetic sea states, a smaller rotor is more efficient. The figures also show that the biradial turbine is less sensitive to changes in the rotor diameter for the more energetic sea states.

5.1.1. Comparison of the Wells and biradial turbines installed at the Mutriku power plant

The characteristics of the Wells and biradial turbines tested at Mutriku are presented in Table 2. They have different diameters and generator rated powers. The turbines are of different types and rotor diameter is not to be compared, only the performance.

From Fig. 11a we found that the biradial turbine with a diameter of $D = 0.50$ m has a CWR_{pneu} 32% lower than the optimal value with $D = 0.85$ m, meaning that the turbine damping is far from optimal. It should be recalled that the biradial turbine tested at the Mutriku power plant was designed to be installed at the IDOM's Marmok A5 OWC spar buoy subject to substantially larger pressure heads. Nevertheless, the CWR_{pneu} of the Wells turbine is only 8% higher than that of the biradial turbine for the base case.

Comparing the CWR_{turb} and the CWR_{elec} of the Wells and biradial turbines, we found that they have similar values although the CWR_{pneu} is considerably smaller for the biradial turbine. This demonstrates that the annual-averaged biradial turbine efficiency is larger in comparison with the Wells turbine, as seen in Fig. 11d. From Fig. 11d we found that a biradial turbine has a computed annual-averaged efficiency of $\bar{\eta}_{turb} = 0.62$ while a Wells turbine has only $\bar{\eta}_{turb} = 0.47$.

5.2. Sensitivity analysis to the control law parameters a and b

Figs. 13 and 14 show the sensitivity of the pneumatic power, turbine power, electrical power and turbine efficiency to the variation of the parameters a and b of the generator control law, Eq. (23), for sea states 5, 7 and 10. All plots are in semi-logarithmic scale. The computations were performed for the base cases with a generator of $P_{gen}^{\text{rated}} = 18.5$ kW. Typically, the Wells turbine rotor should be considerably larger in comparison with the biradial turbine [19]. This is not the case for the Mutriku power plant due to the low-pressure head available to the

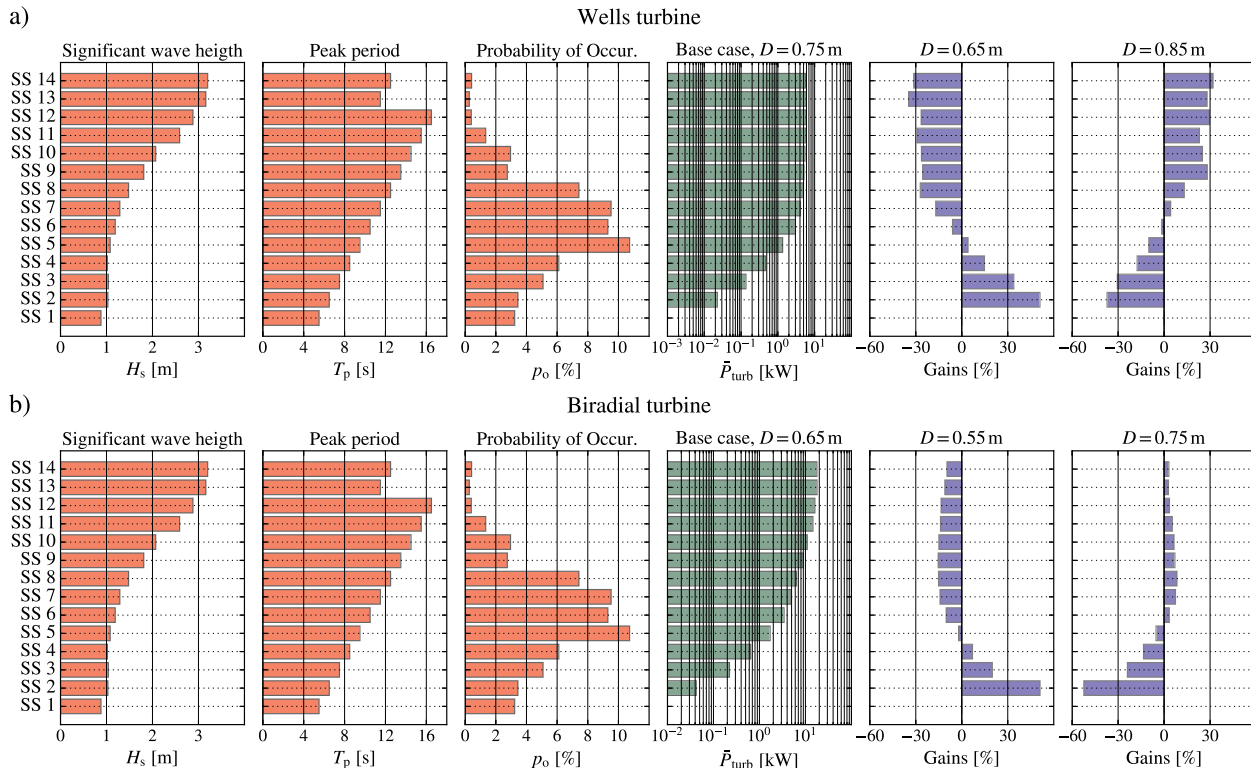


Fig. 12. a) Wells turbine performance for the reference case with a diameter of $D = 0.75$ m, as a function of the sea states of the wave climate, and relative gain comparison with turbine diameters $D = \{0.65, 0.75\}$ m. b) The same as case a) but for the biradial turbine. The biradial turbine reference case has a diameter of $D = 0.65$ m. The comparison cases are for diameters $D = \{0.55, 0.75\}$ m. In all cases the generator had a rated power of 18.5 kW and a maximum rotational speed of 4000 rpm.

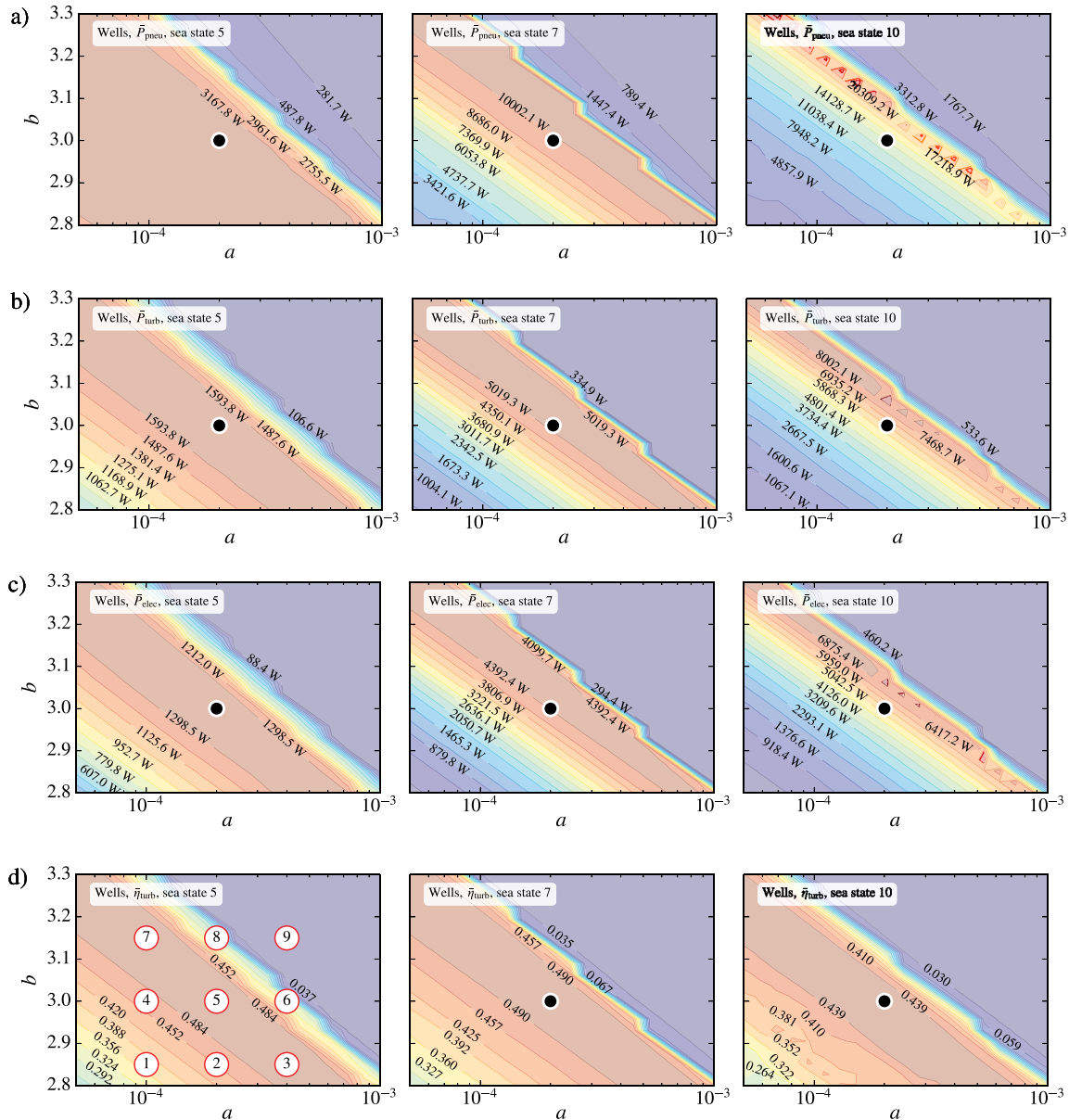


Fig. 13. Time-averaged pneumatic power, turbine power, generator power and turbine efficiency for the Wells turbine, as function of the parameters a and b of the generator control law, Eq. (23). The plots are for sea states 5, 7 and 10 of the wave climate off the Mutriku. The depicted black dot corresponds to the best-efficiency-plot parameters $a = a_{\text{beep}}$ and $b = 3$. The nine points depicted in d) are used in section 5.3.

biradial turbine. The sequence of sea state 5, 7 and 10 are on increasing available wave power order. Note that the plots for the Wells and the biradial turbines do not have the same range for the parameter a since the turbines are of different types. In all plots, the black dots show the pair of a and b corresponding to the best efficiency point, see Eq. (21).

At first glance, there is a major difference between both turbines. There is a sharp drop in the pneumatic and turbine powers of the Wells turbine for larger values of a and b . In contrast, the biradial turbine has a very smooth behaviour and exhibits a broad range of values within which the maximum pneumatic and turbine powers can be attained. This smooth behaviour of the biradial turbine can be explained through two features. On the one hand, the turbine has a relatively smooth efficiency curve, as seen in Fig. 8, in comparison with the sharp drop in efficiency of the Wells turbine above a critical Ψ , Fig. 8. On the other hand, from Eq. (34) we find that the biradial turbine has lower rotational speeds and, consequently, the safety valve is less frequently actuated than for the Wells turbine, see Fig. 9. The effect of the valve actuation is seen in Fig. 13 for sea state 10. With the increase of the

wave power, the efficiency loses the smooth behaviour shown for sea state 5 to a very irregular pattern depicted in sea state 10. By limiting the generator power to the maximum value of $P_{\text{gen}}^{\text{rated}}$, we are also allowing both turbines to achieve higher rotational speeds thus increasing the possibility of actuation of the safety valve, see Fig. 10c. In the case of the Wells turbine, the lower inertia promotes higher rotational accelerations.

The low sensitivity of the power outputs to the generator control law is an essential feature of the biradial turbine, in comparison with the Wells turbine. The range of a and b with high efficiency decreases for the Wells turbine with the increase of the wave power. The opposite occurs for the biradial turbine: with the wave power increase, the region of a and b with high-efficiency increases. For both turbines, the maximum time-averaged efficiency decreases when the wave power increases. This behaviour is expectable since the amplitude of the pressure fluctuations are increasing thus increasing the operating range of Ψ due to the inertia of the rotating parts, and the safety valves operate more often.

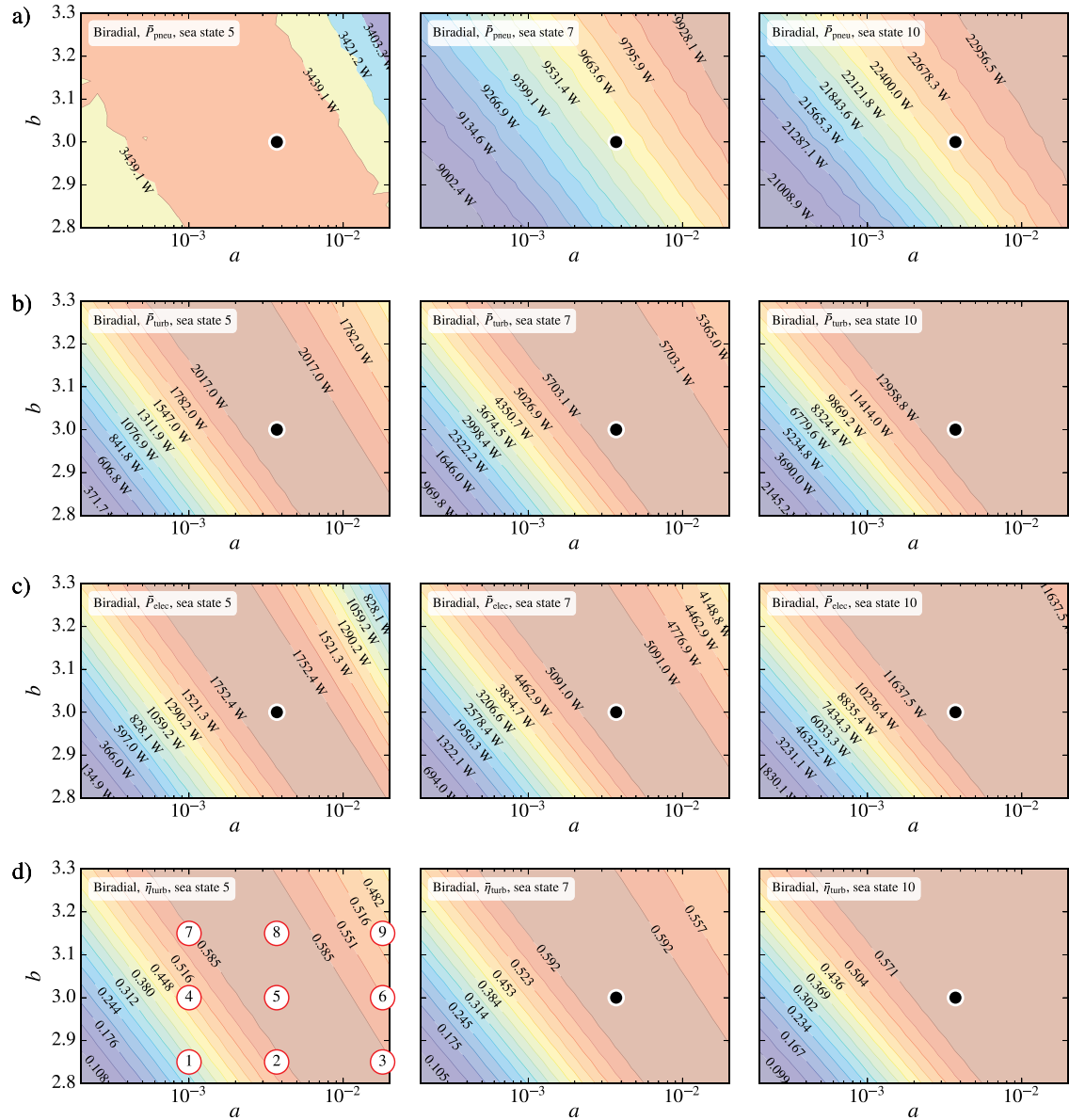


Fig. 14. As in Fig. 13 but for the biradial turbine.

5.3. Turbine operating conditions

The meaning of the results plotted in Figs. 13 and 14 is not entirely obvious. These plots show that there is a relatively broad range of values of the control parameters a and b where the PTO operates in similar conditions. The justification for this behaviour can be found through a statistical analysis of the time-series of the turbine efficiency. Without loss of generality, let us consider nine operating points for sea state 5, as depicted in Figs. 13d and 14d. In the following rationale, several considerations must be taken into account. The generator control laws can follow different paths as shown in Fig. 10c. Changing the generator control law parameters, a and b , implies different instantaneous rotational speeds thus affecting: the turbine operating point through the dimensionless pressure head Ψ and, in the case of the Wells turbine, also changes in the damping, Eq. (32). The biradial turbine damping is marginally affected by the rotational speed, Eq. (34).

For the following statistical analysis, we consider nine operating points depicted in Figs. 13 and 14 for the Wells and biradial turbines base case, respectively. Figs. 15 and 16 depict the frequency of occurrence of Ψ and the turbine efficiency for the nine operating points, as a

function of Ψ , for the Wells and biradial turbines. These figures show that the frequencies of occurrence of Ψ are similar for the sets of operating points {2,4}, {3,5,7} and {6,8}. Moreover, there are three basic types of turbine operating conditions illustrated by points 1, 5 and 9. This classification is independent of the turbine type. The best performance was obtained for point 5, where the values of Ψ are mainly within the range of $0 \leq \Psi \leq \Psi_{\text{bep}}$ corresponding to the higher turbine efficiencies.

Operating point 1 corresponds to an operating condition where the generator torque is lower than at operating point 5. When the generator torque is lower the turbine rotational speed is higher and, for similar pressure heads Δp , the Ψ operating range will be narrower since $\Psi \propto \Omega^{-2}$. The Wells turbine also shows a high probability of occurrence of $\Phi = 0$ due to the increased number of times that the safety valve is operated under low generator torque conditions, see Fig. 15. This effect is of less importance for the biradial turbine because the rotor inertia is an order of magnitude higher and the typical rotational speed is half that of the Wells turbine [11,19].

In contrast to operating point 1, point 9 corresponds to higher generator torques and lower rotational speeds, in comparison with

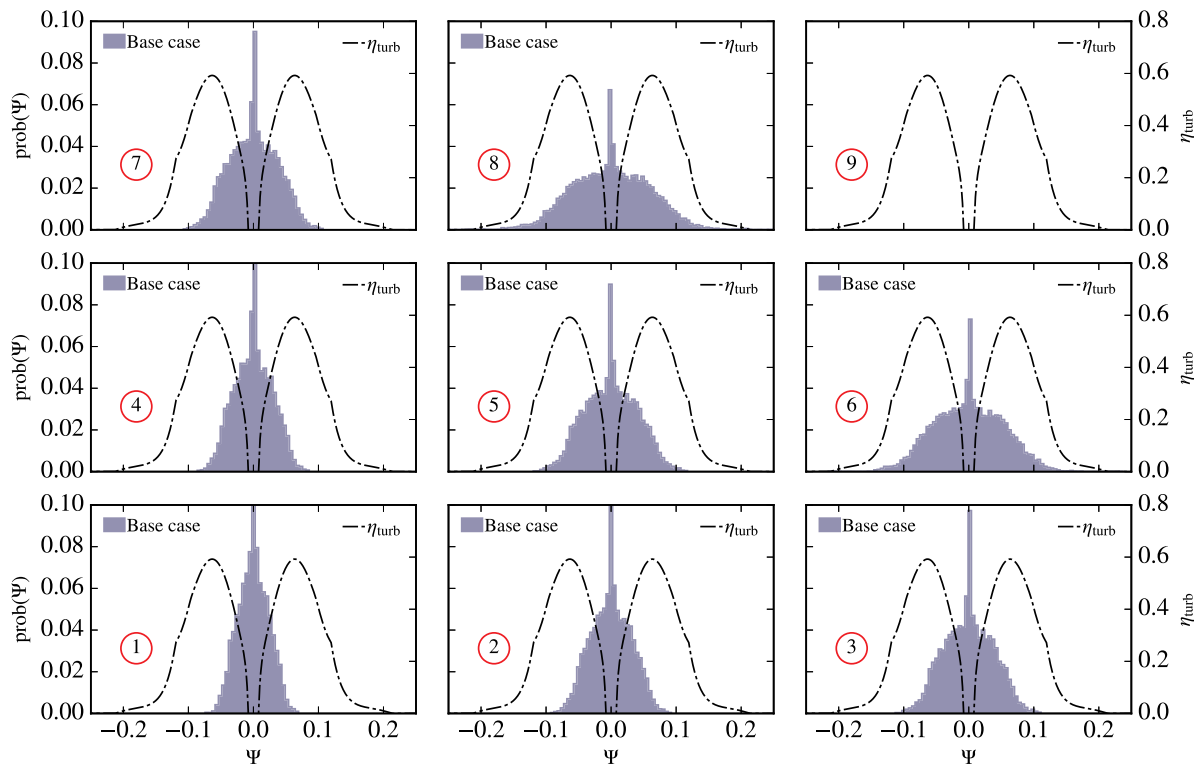


Fig. 15. Distribution of the probability of occurrence of Ψ for the nine operating points depicted in Fig. 13 of sea state 5. For the ease of analysis, it is also plotted the Wells turbine efficiency. Note that the x-axis range is different for operating points 8 and 9. The peak values at $\Psi = 0$ were clipped for points 1, 2 and 4 to reduce the vertical scale.

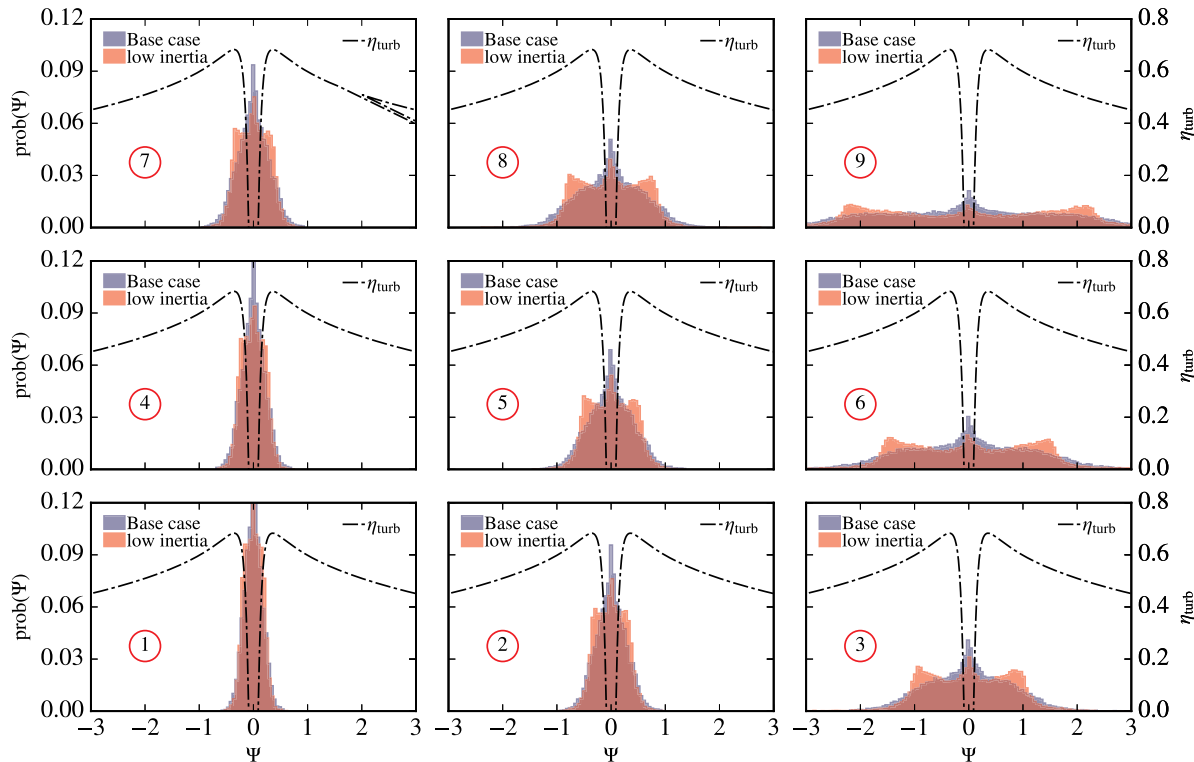


Fig. 16. As in Fig. 15 but for the biradial turbine. The low inertia biradial turbine has an inertia value equal to the Wells turbine base case (about six times smaller). The nine operating points are depicted in Fig. 14d. The peak values at $\Psi = 0$ were clipped for points 1 and 4 to reduce the vertical scale.

point 5. For lower rotational speeds, the Ψ operating range is broader than those for points 1 and 5. The larger operating range of Ψ has a significant effect on the performance of the Wells turbine since it starts to operate under stall conditions. This is seen in Fig. 13, where there is a cliff that separates the regions of high and low efficiencies.

In the case of the Wells turbine, the rotational speed also affects the turbine damping K_W , but this is a second-order effect in comparison with the changes in the turbine operating point Ψ , since $K_W \propto \Omega^{-1}$ and $\Psi \propto \Omega^{-2}$. The available pressure head Δp is expected to increase when the turbine damping decreases. The damping variation with the rotational speed may improve the Wells turbine performance slightly by modifying the operating point as $\Psi \propto \Delta p$. The turbine damping decrease with the increase of the rotational speed tends to increase Ψ for point 1 and thus to improve the overall turbine performance. For point 9, the Wells turbine stalls and stops shortly after the starting of the computations due to excessive generator torque, T_{ctrl}^{lim} , at low rotational speeds. Since no asymptotic data for $\Pi(\Psi)$ and $\Phi(\Psi)$ is available when $\Psi \rightarrow \infty$, the numerical model cannot simulate the self-starting capabilities of the turbine. By using Eq. (24) instead of Eq. (23), we avoid the division by zero when the turbine stops rotating. On the other hand, the biradial turbine shows for operating point 9 a large operating range for Ψ in comparison with operating points 1 and 5.

Figs. 15 and 16 also reveal that the shape of the distribution of the probability of occurrence of Ψ is not symmetric. This shows that the pressure oscillations are not equal for the inhalation and exhalation cycles due to the air compressibility in the chamber.

For the selected diameter, the inertia of the Wells and biradial turbines are 3.06 kg m^2 and 18.6 kg m^2 , respectively. As such, the biradial turbine has slower dynamics in comparison with the Wells turbine. The effect of the turbine inertia in the distribution of the probability of occurrence of Ψ can be seen by comparing the two probability distributions in Fig. 16. The low inertia biradial turbine case corresponds to the inertia of the Wells turbine base case (about six times smaller than the biradial base case). The plots show that the inertia has a significant effect on the performance of the turbine. The distribution of the probability of occurrence of Ψ has a smaller operating range for the lower inertia turbine for similar operating points. As expected, the

lower inertia turbine adjusts faster to the instantaneous operating conditions and improves the time-average turbine efficiency. This was the assumption used to derive Eq. (20).

The different turbine dampings and the effect of the air compressibility is also visible in Fig. 17a and b). Operating points 1, 5 and 9 have different pressure head responses although the wave diffraction force $F_{\text{di}}(t)$ is the same for all cases. The memory effect of the radiation and the compressibility have a strong effect on the response of an OWC system. Comparing the efficiency plots for both turbines reveals the reason for the larger time-averaged efficiency of the biradial turbine. For the case of operating point 5, the biradial turbine operates most of the time close to the best efficiency point, whereas the Wells turbine exhibits an irregular behaviour.

5.4. Power matrices

The variation of the turbine aerodynamic power are depicted in Fig. 18a and b), as a function of the peak period, T_p , and significant wave height, H_s . Again, we are comparing the base case of both turbines, see Table 2. Results presented for the higher values of H_s should be considered as qualitative, due to the assumptions made in the model related to small-amplitude motion conditions. This is inherent to the linear wave theory.

From the analysis of the plots, we found that, due to the higher rotational speed achieved by the Wells turbine, the power output is highly penalized by the closure of the safety valve, in comparison with the biradial turbine, as a consequence of the clipping of the generator control law Eq. (23). Due to the operation of the safety valve for higher energetic sea states, the time-averaged power isolines of the Wells turbine, Fig. 18a, have an irregular pattern not found in the biradial turbine, Fig. 18b. There is also a region for the Wells turbine where the operation was most of the time under stalled conditions, $H_s > 3.5 \text{ m}$ and $12 \text{ s} \leq T_e \leq 13 \text{ s}$.

From the figures, we found that, for peak periods between $10 \text{ s} < T_p < 16.5 \text{ s}$, the capture width depends only on the significant wave height. This fact results from the hydrodynamic response plotted in Fig. 4b, where the power plant always operates in resonance

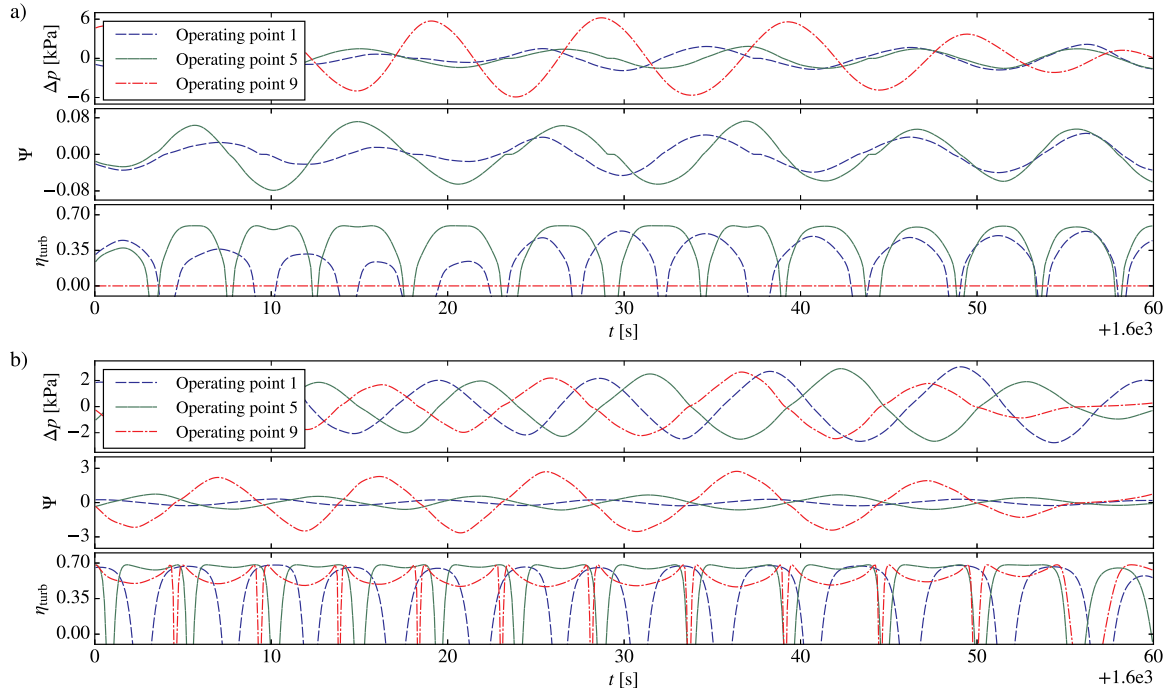


Fig. 17. Time-series of the pressure head Δp , dimensionless pressure head Ψ , and turbine efficiency for the Wells turbine a), and the biradial turbine b). The operating points 1, 5 and 9 are depicted in Fig. 13d for the Wells turbine, and in Fig. 14d for the biradial turbine.

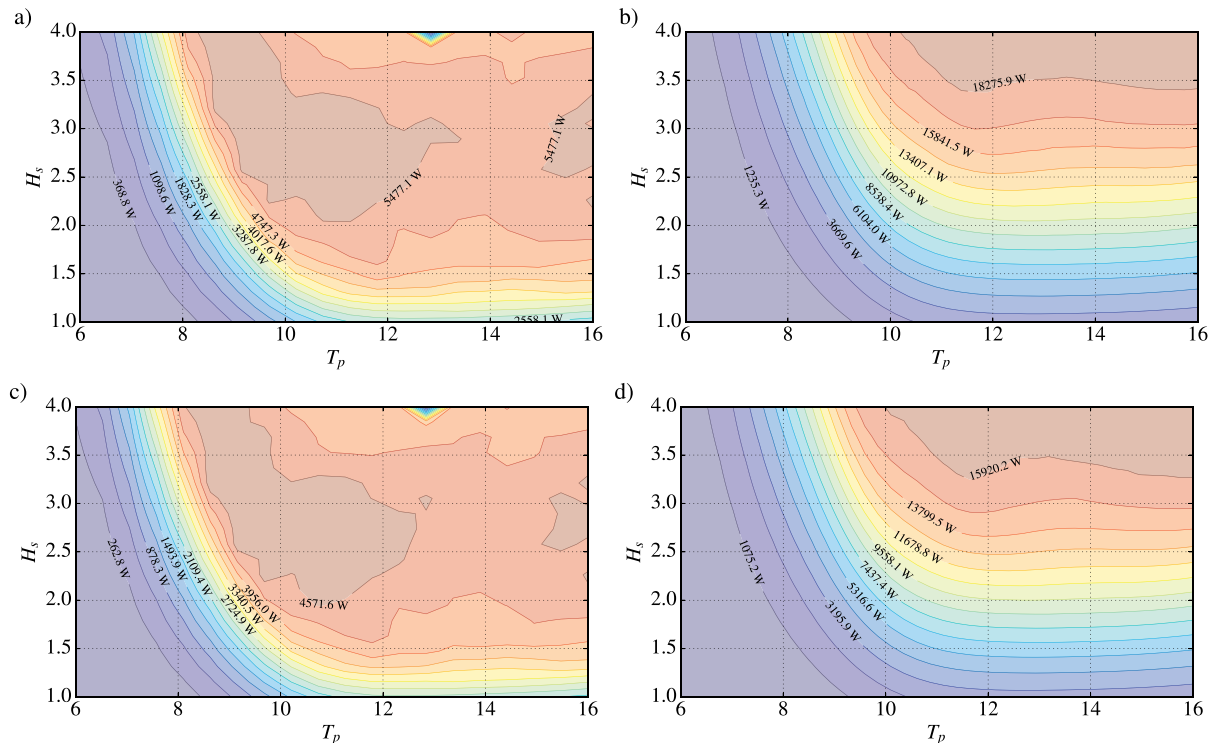


Fig. 18. Time-averaged turbine power matrices for the a) Wells turbine and b) Biradial turbine. Time-averaged electrical power matrices for the c) Wells turbine and d) Biradial turbine.

conditions.

The Wells turbine shows a large plateau with a maximum value around 5.5 kW while the biradial has a smaller plateau with a maximum value about 18.3 kW, a value close the generator rated power of 18.5 kW. The biradial turbine has the capability of operating for long periods at the generator rated power.

The power matrices for the generator are plotted in Fig. 18c and d. As expected, they follow the behaviour of both turbines although the efficiency of the generator decays significantly when the turbine power is much lower than the generator rated power, see Fig. 10d.

6. Conclusions

The present paper aims at comparing the performance of two air turbines at Mutriku OWC-breakwater. A biradial turbine and a Wells turbine were chosen for this purpose, and the analysis was focused on the control parameters sensitivity for pneumatic power, turbine power, electrical power and turbine efficiency. Results show that the Wells turbine performance is far more sensitive to control parameters of the generator, in comparison to the case of the biradial turbine. The biradial turbine has a broad region where the control parameters achieve close to maximum power output in contrast to the relatively smaller range allowed for the Wells turbine.

The biradial turbine has two main advantages over the Wells turbine: a higher peak efficiency and absence of hard-stall characteristics. As such, the biradial turbine can operate close to the highest annual-averaged efficiency within a broad range of the generator control law parameters. For the Mutriku power plant, the biradial turbine presented annual-averaged efficiency 32% higher than the Wells turbine the selected base cases. It should be noted that in this comparison the biradial turbine was not designed for this power plant but to the IDOM's Marmok A5 OWC spar buoy, a device with significantly larger pressure heads.

The instantaneous rotational speed has a stronger impact on the performance of the Wells turbine in comparison with the biradial

turbine. In the case of the Wells turbine the rotational speed determines both the turbine operating point and the damping. For the biradial turbine, the rotational speed sets the operating point but the damping weakly depends on the rotational speed.

The effect of the control parameters upon the instantaneous performance of the turbines was also discussed. Due to the hard-stall aerodynamic characteristics of the Wells turbine, the generator control law must ensure the operation within a rather strict rotational speed interval that also depends on the available instantaneous pressure head. The rotational speed of the Wells turbine is typically twice the value of the biradial turbine for the same sea climate and power level. For higher rotational speeds, the safety valve needs to be actuated to maintain the physical integrity of the turbine rotor. Therefore, the operation of the safety valve installed in series with the rotor has a more significant impact on the Wells turbine than on the biradial turbine. Unlike for optimal control, where the generator control law is tuned wave-by-wave, the performance analysis of any feedback control law should also be performed considering a statistical analysis based on the probability of occurrence of the dimensionless pressure head. For the Wells turbine, the turbine efficiency loss caused by operation away of the best efficiency point is more important than the damping deviation from optimal value due to non-optimal rotational speed.

Another important conclusion is that the selection of the control law is tightly related to the efficiency of the selected generator. The generator should have the maximum efficiency along the operating path of the control law that maximizes the turbine power output. In contrast with the Wells turbine, the biradial turbine has the capability of operating for long periods at the generator rated power.

Acknowledgements

This research was partially supported by: i) FCT (Foundation for Science and Technology), Portugal, through IDMEC (Institute of Mechanical Engineering), under LAETA, project UID/EMS/50022/2019; ii) European Union's Horizon 2020 research and innovation

programme under grant agreement No 654444 (OPERA Project); and iii) WAVEBUOY project - Wave-powered oceanographic buoy for long-term deployment - PTDC/MAR-TEC/0914/2014. The first author was funded by FCT researcher grant No. IF/01457/2014. The fifth author

was funded by Science Foundation Ireland (SFI) Centre for Marine and Renewable Energy Research (MaREI), Grant No. 12/RC/2302. The authors would like to thank François-Xavier Faÿ for giving information about function plotted in Fig. 2 in the early stages of the work.

Appendix A. Wave spectra modelling

The JONSWAP spectra used in the presented computations is described by

$$S_J(\omega) = A_{\gamma_s} \gamma_s^a S_{PM}(\omega), \quad (A.1)$$

where the parameter A_{γ_s} is a normalizing factor given by

$$A_{\gamma_s} = 1 - 0.287 \ln(\gamma_s). \quad (A.2)$$

Here, a spectrum sharpness parameter of $\gamma_s = 2.8$ was used. The exponent a is parameter defined by

$$a = \exp\left(-\frac{(\omega - \omega_p)^2}{2\omega_p^2\sigma^2}\right), \quad (A.3)$$

with

$$\sigma = \begin{cases} 0.07, & \text{if } \omega \leq \omega_p \\ 0.09, & \text{if } \omega > \omega_p \end{cases}. \quad (A.4)$$

and $S_{PM}(\omega)$ is the Pierson-Moskowitz spectra,

$$S_{PM}(\omega) = \frac{5}{16} \frac{H_s^2 \omega_p^4}{\omega^5} \exp\left(-\frac{5}{4}\left(\frac{\omega_p}{\omega}\right)^4\right). \quad (A.5)$$

This spectrum is a function of the significant wave height, H_s , and the peak frequency, ω_p , computed as function of the peak period $T_p = 2\pi/\omega_p$.

Appendix B. Real-valued implementation of the Prony method

The convolution integral appearing in Eq. (6) was approximated by a Prony method [57]. The method starts by approximating the kernel with a sum of exponential functions

$$K(t) = \sum_{k=1}^p \alpha_k e^{\beta_k t}, \quad (B.1)$$

where α_k and β_k are both real or a complex conjugate pair such that

$$\begin{cases} \alpha_1 = \alpha_{12}^{re} + \alpha_{12}^{im} i \\ \beta_1 = \beta_{12}^{re} + \beta_{12}^{im} i \end{cases}, \quad \begin{cases} \alpha_2 = \alpha_{12}^{re} - \alpha_{12}^{im} i \\ \beta_2 = \beta_{12}^{re} - \beta_{12}^{im} i \end{cases}, \quad (B.2)$$

see Ref. [58]. In all cases, the real part β_{12}^{re} is always negative since the $K(t) \rightarrow 0$ when $t \rightarrow \infty$.

Applying Eqs. (B.1) to (6) gives

$$\int_0^t K(t-\tau) \dot{x}(\tau) d\tau = \sum_{k=1}^p \int_0^t \alpha_k e^{\beta_k(t-\tau)} \dot{x}(\tau) d\tau. \quad (B.3)$$

By differentiating Eq. (B.3) in order to time, the convolution integral can be transformed in a differential equation by the use of the well known Leibniz's rule results in

$$\sum_{k=1}^p \frac{d}{dt} \left(\int_0^t \alpha_k e^{\beta_k(t-\tau)} \dot{x}(\tau) d\tau \right) = \sum_{k=1}^p \left(\int_0^t \alpha_k \beta_k e^{\beta_k(t-\tau)} \dot{x}(\tau) d\tau + \alpha_k \dot{x}(t) \right). \quad (B.4)$$

Defining

$$I_k = \int_0^t \alpha_k e^{\beta_k(t-\tau)} \dot{x}(\tau) d\tau, \quad (B.5)$$

Eq. (B.4) can be expressed as

$$\sum_{k=1}^p \dot{I}_k = \sum_{k=1}^p (\beta_k I_k + \alpha_k \dot{x}(t)). \quad (B.6)$$

Using the principle of superposition, the differential Eq. (B.6) can be solved as a system of equations of the form

$$\dot{I}_1 = \beta_1 I_1 + \alpha_1 \dot{x}(t), \quad (B.7a)$$

$$\dot{I}_2 = \beta_2 I_2 + \alpha_2 \dot{x}(t), \quad (B.7b)$$

...

$$\dot{I}_m = \beta_m I_m + \alpha_m \dot{x}(t). \quad (\text{B.7c})$$

In present work, the following matricial form of Eq. (B.7) was adopted

$$\dot{\mathbf{I}}_r = \boldsymbol{\beta}_r \mathbf{I}_r + \boldsymbol{\alpha}_r \dot{\mathbf{x}}_l. \quad (\text{B.8})$$

Assuming, for example, that α_1 and α_2 , as well as β_1 and β_2 , are conjugate pairs as in Eq. (B.2), the numerical solution of the differential Eqs. (B.7a) and (B.7b) requires the use of complex numbers. However, Eqs. (B.7a) and (B.7b) can be manipulated to give a set of two real differential equations. Since the radiation term, R , is always real, the terms I_1 and I_2 must be a conjugate pair

$$\begin{aligned} I_1 &= I_{12}^{\text{re}} + I_{12}^{\text{im}} i, \\ I_2 &= I_{12}^{\text{re}} - I_{12}^{\text{im}} i, \end{aligned} \quad (\text{B.9})$$

and Eqs. (B.7a) and (B.7b) can be written in the form

$$\begin{aligned} \dot{I}_{12}^{\text{re}} + I_{12}^{\text{im}} i &= \beta_1 I_1 + \alpha_1 \dot{x}(t), \\ \dot{I}_{12}^{\text{re}} - I_{12}^{\text{im}} i &= \beta_2 I_2 + \alpha_2 \dot{x}(t). \end{aligned} \quad (\text{B.10})$$

Solving in order to the real and imaginary parts gives

$$\begin{aligned} \dot{I}_{12}^{\text{re}} &= \beta_{12}^{\text{re}} I_{12}^{\text{re}} - \beta_{12}^{\text{im}} I_{12}^{\text{im}} + \alpha_{12}^{\text{re}} \dot{x}(t), \\ \dot{I}_{12}^{\text{im}} &= \beta_{12}^{\text{im}} I_{12}^{\text{re}} + \beta_{12}^{\text{re}} I_{12}^{\text{im}} + \alpha_{12}^{\text{im}} \dot{x}(t). \end{aligned} \quad (\text{B.11})$$

The contribution of I_1 and I_2 for the radiation term, R , is compute from

$$I_1 + I_2 = 2I_{12}^{\text{re}}. \quad (\text{B.12})$$

Finally, the radiation term is simply evaluated as

$$R = \sum_{k=1}^p I_k. \quad (\text{B.13})$$

References

- [1] Falcão A F de O. Wave energy utilization: a review of the technologies. *Renew Sustain Energy Rev* 2010;14(3):899–918. <https://doi.org/10.1016/j.rser.2009.11.003>.
- [2] Clément A, McCullen P, Falcão AFO, Fiorentino A, Gardner F, Hammarlund K, Lemonis G, Lewis T, Nielsen K, Petroncini S, Pontes MT, Schild P, Sjöström B-O, Sørensen HC, Thorpe T. Wave energy in europe: current status and perspectives. *Renew Sustain Energy Rev* 2002;6(5):405–31. [https://doi.org/10.1016/S1364-0321\(02\)00009-6](https://doi.org/10.1016/S1364-0321(02)00009-6).
- [3] López I, Andreu J, Ceballos S, de Alegría IM, Kortabarria I. Review of wave energy technologies and the necessary power-equipment. *Renew Sustain Energy Rev* 2013;27:413–34. <https://doi.org/10.1016/j.rser.2013.07.009>.
- [4] Mustapa MA, Yaakob OB, Ahmed YM, Rheem C-K, Koh KK, Adnan FA. Wave energy devices and breakwater integration: a review. *Renew Sustain Energy Rev* 2017;77:43–58. <https://doi.org/10.1016/j.rser.2017.03.110>.
- [5] Korda UA, Ringwood JV. Hydrodynamic control of wave energy devices. UK: Cambridge University Press; 2016. <https://doi.org/10.1017/CBO9781139942072>.
- [6] Folley M, editor. Numerical modelling of wave energy converters: state-of-the-art techniques for single devices and arrays. UK: Academic Press; 2016.
- [7] IEA-OES. IEA-Ocean energy systems: annual report 2002 Technical report Ocean Energy Systems; 2002. https://wwwocean-energy-systems.org/documents/70757_ieaoes_annual_report_2002.pdf/.
- [8] OES. Annual report: an overview of ocean energy activities in 2017 Technical report Ocean Energy Systems; 2018. <https://wwwocean-energy-systems.org/documents/53215-oes-annual-report-2017.pdf/>.
- [9] Sener SEC, Sharp JL, Antclif A. Factors impacting diverging paths of renewable energy: a review. *Renew Sustain Energy Rev* 2018;81:2335–42. <https://doi.org/10.1016/j.rser.2017.06.042>.
- [10] Heath TV. A review of oscillating water columns. *Phil Trans Roy Soc Lond A: Math Phys Eng Sci* 1959;370:235–45. <https://doi.org/10.1098/rsta.2011.0164>. 2012.
- [11] Falcão AFO, Henriques JCC. Oscillating-water-column wave energy converters and air turbines: a review. *Renew Energy* 2016;85:1391–424. <https://doi.org/10.1016/j.renene.2015.07.086>.
- [12] Delmonte N, Barated D, Giuliani F, Cova P, Buticchi G. Oscillating water column power conversion: a technology review. 2014 IEEE energy conversion congress and exposition (ECCE) 2014. p. 1852–9. <https://doi.org/10.1109/ECCE.2014.6953644>.
- [13] Falcão AFO, Gato LMC. Air turbines. Sayigh A, editor. Comprehensive renewable energy, vol. 8. Oxford: Ocean Energy, Elsevier; 2012. p. 111–49. <https://doi.org/10.1016/B978-0-08-087872-0-00805-2>.
- [14] Raghunathan S. The Wells air turbine for wave energy conversion. *Prog Aero Sci* 1995;31(4):335–86. [https://doi.org/10.1016/0376-0421\(95\)00001-F](https://doi.org/10.1016/0376-0421(95)00001-F).
- [15] Setoguchi T, Takao M. Current status of self rectifying air turbines for wave energy conversion. *Energy Convers Manag* 2006;47(15–16):2382–96. <https://doi.org/10.1016/j.enconman.2005.11.013>.
- [16] Curran R, Folley M. Air turbine design for OWCs. In: Cruz J, editor. Ocean wave energy - current status and future prospects. Berlin: Springer-Verlag; 2008. p. 189–219. https://doi.org/10.1007/978-3-540-74895-3_6.
- [17] Falcão AFO, Gato LMC, Nunes EPAS. A novel radial self-rectifying air turbine for use in wave energy converters. *Renew Energy* 2013;50:289–98. <https://doi.org/10.1016/j.renene.2012.06.050>.
- [18] Falcão AFO, Gato LMC, Nunes EPAS. A novel radial self-rectifying air turbine for use in wave energy converters. Part 2. Results from model testing. *Renew Energy* 2013;53:159–64. <https://doi.org/10.1016/j.renene.2012.11.018>.
- [19] Falcão AFO, Henriques JCC, Gato LMC. Self-rectifying air turbines for wave energy conversion: a comparative analysis. *Renew Sustain Energy Rev* 2018;91:1231–41. <https://doi.org/10.1016/j.rser.2018.04.019>.
- [20] Budal K, Falnes J. Optimum operation of improved wave power converter. *Mar Sci Commun* 1977;3:133–50.
- [21] Falnes J. Ocean waves and oscillating systems. Cambridge, UK: Cambridge University Press; 2002. <https://doi.org/10.1017/CBO9780511754630>.
- [22] Falnes J. Optimum control of oscillation of wave-energy converters. *Int J Offshore Polar Eng* 2002;12:147–55.
- [23] Sarmento JNA. Model-test optimization of an OWC wave power plant. *Int J Offshore Polar Eng* 1993;2:66–72.
- [24] Babarit A, Clément AH. Optimal latching control of a wave energy device in regular and irregular waves. *Appl Ocean Res* 2006;28:77–91. <https://doi.org/10.1016/j.apor.2006.05.002>.
- [25] Cândido JJ, Justino PAPS. Modelling, control and Pontryagin maximum principle for a two-body wave energy devices. *Renew Energy* 2011;36(5):1545–57. <https://doi.org/10.1016/j.renene.2010.11.013>.
- [26] Lopes MFP, Hals J, Gomes RPF, Moan T, Gato LMC, Falcão A F de O. Experimental and numerical investigation of non-predictive phase-control strategies for a point-absorbing wave energy converter. *Ocean Eng* 2009;36(5):386–402. <https://doi.org/10.1016/j.oceaneng.2009.01.015>.
- [27] Henriques JCC, Falcão AF de O, Gomes RPF, Gato LMC. Latching control of an OWC spar buoy wave energy converter in regular waves. Proceedings of the 31st International conference on ocean, 135. Offshore and Arctic Engineering; 2013. p. 641–50. <https://doi.org/10.1115/OMAE2012-83631>. 2.
- [28] Henriques JCC, Gato LMC, Falcão AFO, Robles E, Faÿ F-X. Latching control of a floating oscillating-water-column wave energy converter. *Renew Energy* 2016;90:229–41. <https://doi.org/10.1016/j.renene.2015.12.065>.
- [29] Henriques JCC, Gato LMC, Lemos JM, Gomes RPF, Falcão AFO. Peak-power control of a grid-integrated oscillating water column wave energy converter. *Energy* 2016;109:378–90. <https://doi.org/10.1016/j.energy.2016.04.098>.
- [30] Henriques JCC, Lemos JM, Eça L, Gato LMC, Falcão AFO. A high-order Discontinuous Galerkin Method with mesh refinement for optimal control. *Automatica* 2017;85:70–82. <https://doi.org/10.1016/j.automatica.2017.07.029>.
- [31] Henriques JCC, Lemos JM, Eça L, Valério JNH, Gato LMC, Falcão AFO. A Discontinuous Galerkin Method for optimal and sub-optimal control applied to an oscillating water column wave energy converter. *IFAC-PapersOnLine* 2017;50(1):15670–7. <https://doi.org/10.1016/j.ifacol.2017.08.2400>.
- [32] Mishra SK, Purwar S, Kishor N. Maximizing output power in oscillating water

- column wave power plants: an optimization based MPPT algorithm. *Technologies* 2018;6(1). <https://doi.org/10.3390/technologies6010015>.
- [33] Rajapakse G, Jayasinghe S, Fleming A, Negnevitsky M. A model predictive control-based power converter system for oscillating water column wave energy converters. *Energies* 2017;10(10). <https://doi.org/10.3390/en10101631>.
- [34] S. K. Song, J. B. Park, Control strategy of an impulse turbine for an oscillating water column-wave energy converter in time-domain using Lyapunov stability method, *Appl Sci* 6 (10), 281. doi:10.3390/app6100281.
- [35] Sheng W, Lewis A. Power takeoff optimization to maximize wave energy conversions for oscillating water column devices. *IEEE J Ocean Eng* 2018;43(1):36–47. <https://doi.org/10.1109/JOE.2016.2644144>.
- [36] M'zoughi F, Bouallègue S, Garrido AJ, Garrido I, Ayadi M. Stalling-free control strategies for oscillating-water-column-based wave power generation plants. *IEEE Trans Energy Convers* 2018;33(1):209–22. <https://doi.org/10.1109/TEC.2017.2737657>.
- [37] Sheng W, Lewis A. Power takeoff optimization for maximizing energy conversion of wave-activated bodies. *IEEE J Ocean Eng* 2016;41(3):529–40. <https://doi.org/10.1109/JOE.2015.2489798>.
- [38] Mérigaud A, Ringwood JV. Improving the computational performance of nonlinear pseudospectral control of wave energy converters. *IEEE Trans Sustain Energy* 2018;9(3):1419–26. <https://doi.org/10.1109/TSTE.2017.2786045>.
- [39] Ringwood JV, Bacelli G, Fusco F. Energy-maximizing control of wave-energy converters: the development of control system technology to optimize their operation. *IEEE Control Syst* 2014;34(5):30–55. <https://doi.org/10.1109/MCS.2014.2333253>.
- [40] Cantarellas AM, Remon D, Rodríguez P. Adaptive vector control of wave energy converters. *IEEE Trans Ind Appl* 2017;53(3):2382–91. <https://doi.org/10.1109/TIA.2017.2655478>.
- [41] Penalba M, Ringwood JV. A review of wave-to-wire models for wave energy converters. *Energies* 2016;7(9). <https://doi.org/10.3390/en9070506>.
- [42] Henriques JCC, Falcão AFO, Gomes RPF, Gato LMC. Air turbine and primary converter matching in spar-buoy oscillating water column wave energy device. Proceedings of the 32nd international conference on ocean Nantes, France: Offshore and Arctic Engineering; 2013. <https://doi.org/10.1115/OMAE2013-11213>.
- [43] Justino PAP, Falcão A F de O. Rotational speed control of an OWC wave power plant. *J Offshore Mech Arct Eng* 1999;121(2):65–70. <https://doi.org/10.1115/1.2830079>.
- [44] Falcão A F de O. Control of an oscillating-water-column wave power plant for maximum energy production. *Appl Ocean Res* 2002;24(2):73–82. [https://doi.org/10.1016/S0141-1187\(02\)00021-4](https://doi.org/10.1016/S0141-1187(02)00021-4).
- [45] Amundarain M, Alberdi M, Garrido AJ, Garrido I. Neural rotational speed control for wave energy converters. *Int J Control* 2011;84(2):293–309. <https://doi.org/10.1080/00207179.2010.551141>.
- [46] Alberti L, Tedeschi E, Bianchi N, Santos M, Fasolo A. Effect of the generator sizing on a wave energy converter considering different control strategies. *COMPEL - The International Journal for Computation and Mathematics in Electrical and Electronic Eng* 2012;32(1):233–47. <https://doi.org/10.1108/03321641311293867>.
- [47] Ente Vasco de la Energia, <https://www.eve.eus/Actuaciones/Marina?lang=en-gb>, accessed: 2019-02-05.
- [48] Torre-Enciso Y, Ortubia I, López de Aguilera LII, Marqués J. Mutriku wave power plant: from the thinking out to the reality. Proc 8th European wave tidal energy conf. 2009. p. 319–29. Uppsala, Sweden.
- [49] Medina-Lopez E, Allsop W, Dimakopoulos A, Bruce T. Conjectures on the failure of the OWC breakwater at Mutriku. Coastal structures and solutions to coastal disasters, joint conference 2015. <https://doi.org/10.1061/9780784480304.063>. Boston, USA.
- [50] Faÿ F-X, Kelly J, Henriques JCC, Pujana A, Abusara M, Mueller M, Touzon I, Ruiz-Minguela P. Numerical simulation of control strategies at Mutriku wave power plant. Proceedings of the 37th international conference on ocean, offshore and arctic engineering, OMAE 2018 2018. <https://doi.org/10.1115/OMAE2018-78011>. Madrid, Spain.
- [51] Henriques JCC, Lopes MFP, Gomes RPF, Gato LMC, Falcão AFO. On the annual wave energy absorption by two-body heaving WECs with latching control. *Renew Energy* 2012;45:31–40. <https://doi.org/10.1016/j.renene.2012.01.102>.
- [52] Taghipour R, Perez T, Moan T. Hybrid frequency-time domain models for dynamic response analysis of marine structures. *Ocean Eng* 2008;35(7):685–705. <https://doi.org/10.1016/j.oceaneng.2007.11.002>.
- [53] Sheng W, Alcorn R, Lewis A. Assessment of primary energy conversions of oscillating water columns I. Hydrodynamic analysis. *J Renew Sustain Energy* 2014;6(5):053113. <https://doi.org/10.1063/1.4896850>.
- [54] Newman JN, Lee CH. WAMIT user manual. 2016 available online at: <http://www.wamit.com/manual.htm> Last accessed date 2019/2/3.
- [55] Cummins WE. The impulse response function and ship motions. *Schiffstechnik* 1962;47(9):101–9.
- [56] Ogilvie TF. Recent progress towards the understanding and prediction of ship motions. In proc. Fifth symp. on naval hydrodynamics. Washington, D.C.: Office of Naval Research Department of the Navy; 1964. p. 3–128.
- [57] Duclos G, Clement AH, Chatry G. Absorption of outgoing waves in a numerical wave tank using a self-adaptive boundary condition. 10th int. offshore and polar engineering conf. ISOPE2000. 2000. Seattle (USA).
- [58] Sheng W, Alcorn R, Lewis A. A new method for radiation forces for floating platforms in waves. *Ocean Eng* 2015;105:43–53. <https://doi.org/10.1016/j.oceaneng.2015.06.023>.
- [59] Henriques JCC, Gomes RPF, Gato LMC, Falcão AFO, Robles E, Ceballos S. Testing and control of a power take-off system for an oscillating-water-column wave energy converter. *Renew Energy* 2016;85:714–24. <https://doi.org/10.1016/j.renene.2015.07.015>.
- [60] Garrido I, Garrido AJ, Alberdi M, Amundarain M, Barambones O. Performance of an ocean energy conversion system with DFIG sensorless control. *Math Probl Eng* 2013;2013:1–14. <https://doi.org/10.1155/2013/260514>. Article ID 260514.
- [61] Dixon SL, Hall CA. Fluid mechanics and thermodynamics of turbomachinery. seventh ed. Oxford: Butterworth-Heinemann; 2013. <https://www.elsevier.com/books/fluid-mechanics-and-thermodynamics-of-turbomachinery/dixon/978-0-12-415954-9>.
- [62] Dick E. Fundamentals of turbomachines, vol. 109 of fluid mechanics and its applications. Netherlands: Springer; 2015. <https://doi.org/10.1007/978-94-017-9627-9>.
- [63] Tease WK, Lees J, Hall A. Advances in oscillating water column air turbine development. Proceedings of the 7th European wave and tidal energy conference. 2007. Porto, Portugal.
- [64] Gato LMC, Carrelhas AAD, da Fonseca FXC, Henriques JCC. OPERA Deliverable D3.2 - turbine-generator set laboratory tests in variable unidirectional flow, Tech. Rep. Instituto Superior Técnico.; 2017. http://opera-h2020.eu/wp-content/uploads/2016/03/OPERA_D3-2_Dry_Testing_IST.pdf.
- [65] Henriques JCC, Gato LMC. Use of a Residual Distribution Euler solver to study the occurrence of transonic flow in Wells turbine rotor blades. *Comput Mech* 2002;29(3):243–53. <https://doi.org/10.1007/s00466-002-0337-8>.
- [66] Carrelhas AAD. Experimental study of a model and prototype of a self-rectifying bi-radial air turbine with fixed guide vanes, Master's thesis. Portugal: Instituto Superior Técnico, Universidade de Lisboa; 2017. https://fenix.tecnico.ulisboa.pt/downloadFile/1970719973966849/67733_dissertacao.pdf.